International Journal of Solids and Structures 217-218 (2021) 27–39

Contents lists available at ScienceDirect

International Journal of Solids and Structures

journal homepage: www.elsevier.com/locate/ijsolstr

# A collocation mixed finite element method for the analysis of flexoelectric solids

Xinpeng Tian [a,b], Jan Sladek [a,*], Vladimir Sladek [a], Qian Deng [b], Qun Li [b]

[a] Institute of Construction and Architecture, Slovak Academy of Sciences, 84503 Bratislava, Slovakia
[b] State Key Laboratory for Strength and Vibration of Mechanical Structures, School of Aerospace Engineering, Xi'an Jiaotong University, Xi'an 710049, China

ARTICLE INFO

*Article history:*
Received 23 September 2020
Received in revised form 14 December 2020
Accepted 27 January 2021
Available online 09 February 2021

*Keywords:*
Flexoelectricity
collocation MFEM
Gradients of strain and electric intensity vector
Higher efficiency
Geometric dependence

ABSTRACT

A collocation mixed finite element method (MFEM) for direct and converse flexoelectricity in piezoelectric materials is developed for 2D problems. The size-effect phenomenon in micro/nano structures is considered by the strain- and electric intensity vector-gradient effects. $C^0$ continuous finite element method is inadequate to treat flexoelectricity problems involving the size-effect. To this end, the MFEM with Lagrangian multipliers to treat these solids has been reported recently. With existing MFEM, the computational efficiency is low due to the additional nodal degrees of freedom (DOFs) for the Lagrangian multipliers. In this study, a new collocation MFEM is proposed, in which the number of the DOFs, when compared to the traditional Lagrangian approach, can be reduced. At the same time, the kinematic constraints between the displacement and strain are guaranteed. These kinematic constraints are satisfied by the collocation method at some internal points in the finite elements. The present collocation MFEM can be used to solve flexoelectricity problems with higher efficiency. Its accuracy is verified by comparing the numerical results with available analytical solutions for the bending of a cantilever beam and the compression of a truncated pyramid, respectively. The results indicate that flexoelctricity is strongly related to the geometry of the physical problem. It is shown that flexoelectricity increases significantly with the decrease of the sample size. The same occurs when, for the beam problem, the ratio of the length to depth dimensions increases; similarly, for the truncated pyramid problem, when the ratio of the width of the bottom and top surfaces increases.



## 1. Introduction

Recent progress in microelectronics is, in large part, driven by continuous miniaturization of devices and the use of nanotechnologies in which size-dependent effects cannot be ignored. The direct flexoelectric effect describes the coupling between the strain gradients and the electric polarization (Kogan, 1964; Meyer, 1969; Sharma et al., 2006). A non-uniform strain, i.e. the presence of strain gradients, may potentially break the inversion symmetry thereby inducing electric polarization even in centrosymmetric crystals (Tagantsev, 1986; Tagantsev et al., 2009; Maranganti et al., 2006). Flexoelectricity is found to be a universal electromechanical coupling that exists in all dielectric materials even with a centrosymmetric crystal structure (Yudin and Tagantsev, 2013; Deng et al., 2014a, 2014b, 2020). The existence of flexoelectric effect in solids has been observed experimentally as first reported by Harris (1965). However, a systematic measurement of flexoelectricity was only performed a few decades later in the 2000s, see, e.g. Ma and Cross (2001), Ma and Cross (2006). Perspectives on the future directions for research on flexoelectricity are given in some review papers (Krichen and Sharma, 2016; Wang et al., 2019; Zhuang et al., 2020; Deng et al., 2020).

To utilize the flexoelectric effect, the strain gradients have to be relatively large; they are therefore more easily generated in nanoscale structures. The dimensions of such solids are of the same order of the material length scale parameter used in generalized theories of continua. As has been shown experimentally, the stiffness of such a structure increases with a decrease in its size. The presence of strain gradients can also be realized by differences in material properties at the interfaces of these materials even under a uniform stress (Deng et al., 2014a, 2014b).

In order to perform good design of devices with flexoelectric properties, it is necessary to analyze general boundary value problems (BVPs) of these components. It is well-known that classical continuum mechanics neglect the influence of the material microstructure and the results are size-independent. To overcome intrinsic limitations of classical elasticity, atomistic models have

* Corresponding author.
*E-mail address:* jan.sladek@savba.sk (J. Sladek).

https://doi.org/10.1016/j.ijsolstr.2021.01.031
0020-7683/

been developed to describe the micro-scale phenomena in materials. Extremely high requirements on computer memory in these models have led to the development of multiscale approaches where atomistic and continuum subdomains are bridged. Due to intrinsic heterogeneities in the atomistic-continuum coupling, some physically unrealistic phenomena have been observed especially for time-dependent problems. Another approach to treat this problem is based on the phenomenological theory of flexoelectricity within the generalized thermodynamics of a dielectric. This involves introducing a flexoelectric contribution into the total free energy (Tagantsev, 1986). The flexoelectricity can be realized as the direct flexoelectric effect (Sharma et al., 2006; Gharbi et al., 2009), and converse flexoelectricity. The former refers to the linear coupling of electric fields and strain gradients, and it is frequently investigated in the literature. The converse flexoelectricity is the coupling between the stress and applied electric intensity vector gradients (Yang et al., 2004). Maugin (1980) showed the duality between the theory of electric field gradient and the theory of flexoelectricity. Hu and Shen (2009) and Shen and Hu (2010) have extended the general flexoelectric theory by the surface effects for nano-sized elastic dielectrics. They have developed the variational principle for these problems. Recently, flexoelectricity in biological membranes and soft electrets has attracted the attention of several researchers. The corresponding flexoelectric membrane theory and nonlinear flexoelectric theory in electret soft materials have been proposed (Mohammadi et al., 2014; Deng et al., 2014a, 2014b; Rahmati et al., 2019).

For nano-sized flexoelectric structures it is necessary to apply gradient theory in which the governing equations are partial differential equations (PDE) of the fourth order. To solve flexoelectric problems with strain- and electric intensity vector-gradient effects, several numerical methods have been developed, namely, moving least square (MLS) (Sladek et al., 2013), meshfree formuation method (Abdollahi et al., 2014, 2015), isogeometric analysis (IGA) (Thai et al., 2018; Nguyen et al., 2018, 2019; Liu et al., 2019), hierarchical B-spline method (Codony et al., 2019), and finite element method (FEM) (Yvonnet and Liu, 2017; Sladek et al., 2018; Amanatidou and Aravas, 2002; Mao et al., 2016; Deng et al., 2017, 2018).

Among the numerical methods mentioned above, the FEM has been well established as a powerful computational tool for analysing general BVPs with complex geometries. However, the conventional FEM cannot be used to study flexoelectricity due to the strain- and electric intensity vector-gradient effects, where second derivatives of the primary fields (displacement and electric potential) are required. Two modified FEMs to resolve this problem have been reported in the literature. The first approach involves the use of $C^1$ continuity elements. For example, Yvonnet and Liu (2017) have applied $C^1$ Argyris triangular elements for soft flexoelectric solids at finite strains. Sladek et al. (2018) have developed conforming elements with $C^1$ continuity, where each node has 9 degrees of freedom (6 mechanical quantities, electric potential, and two potential gradients) for 2D flexoelectric problems. The $C^1$ continuous element is established by using higher order shape functions. It is, however, difficult to develop $C^1$ elements for 3D problems. Another way to resolve the gradient problem is to use mixed finite element methods (MFEMs) which are relatively more convenient to develop. Following the works of Amanatidou and Aravas (2002) for the MFEM in gradient theory of elasticity, Mao et al. (2016) constructed a MFEM formulation for flexoelectricity with extra nodal degrees-of-freedom (DOFs) for polarizations and developed a 2D element to solve general BVPs. Deng et al. (2017), Deng et al. (2018) have also developed a MFEM with strain gradient and flexoelectricity and extended it to 3D flexoelectricity problems.

In traditional MFEM (Mao et al., 2016; Deng et al., 2017, 2018), the kinematic relationship between displacement field and its gradient is enforced by Lagrangian multipliers. In the formulation, the displacement gradient and Lagrangian multipliers are set as additional nodal DOFs to displacements, electric potential and polarization (Amanatidou and Aravas, 2002; Mao et al., 2016). Therefore, extra DOFs are introduced thereby leading to lower computational efficiency. For example, there are 87 DOFs for a 2D quadrilateral element in formulation by Mao et al. (2016); and the corresponding number is 47 in Deng et al's formulation. This is a significant drawback for analysing large scale models. A new finite element method with greater efficiency would therefore be highly desirable; this is the subject of the present paper.

In this study, a collocation MFEM for direct and converse flexoelectricity in piezoelectric materials is developed. The size-effect is considered by including the strain gradients, electric field gradients, and their coupling in the constitutive equations of the piezoelectric materials. The $C^0$ continuous approximation is applied independently for displacements and strains. The kinematic constraints between strains and displacements are satisfied by collocation method at judiciously chosen internal points of the elements (Dong and Atluri, 2011; Bishay et al., 2012). In contrast, the Lagrange multipliers are used to enforce these kinematic constraints in the traditional MFEM (Amanatidou and Aravas, 2002; Mao et al., 2016). The electric potential and electric intensity vector are approximated by $C^0$ continuity in the same manner. The corresponding constraint between the electric intensity vector and the electric potential are also satisfied by the same collocation method. No extra DOFs are introduced in this collocation MFEM. Thus, there are just 12 DOFs for a 2D quadrilateral element (eight displacements and four potentials). In the case of isogeometric analysis, the non-uniform rational B-spline functions with higher order continuity can be employed; no extra DOFs are therefore needed (Thai et al., 2018), like in the present approach.

A MFEM code based on this formulation is developed in this study and its veracity is demonstrated with two example problems, The first is a simple cantilever beam problem for which the analytical solution is available. The second example is a truncated pyramid under a compressive load. Before discussing these numerical examples, a review of the governing equations in flexoelectricity is perhaps in order. This will be followed by a presentation of the formulation of the proposed collocation MFEM.

## 2. Direct and converse flexoelectricity

The electric enthalpy density for piezoelectric solids can be written as (Maranganti et al., 2006; Hu and Shen, 2009)

$$H = \frac{1}{2}c_{ijkl}\varepsilon_{ij}\varepsilon_{kl} - \frac{1}{2}a_{ij}E_iE_j - e_{kji}\varepsilon_{ij}E_k + \frac{1}{2}g_{jklmni}\eta_{jkl}\eta_{mni} - f_{ijkl}E_i\eta_{jkl} - b_{klij}\varepsilon_{ij}E_{k,l} - \frac{1}{2}h_{ijkl}E_{i,j}E_{k,l} \quad (1)$$

where symbols $\boldsymbol{a}$ and $\boldsymbol{c}$ are used for the second-order permittivity and the fourth-order elastic constant tensors, respectively. The piezoelectric coefficient is denoted by $\boldsymbol{e}$ and $\boldsymbol{f}$ is the direct flexoelectric coefficient. The tensor $\boldsymbol{g}$ is used for higher order elastic coefficients representing the strain-gradient elasticity. The symbols $\boldsymbol{b}$ and $\boldsymbol{h}$ are used for the converse flexoelectric coefficients and higher-order electric parameters, respectively. The strain tensor $\varepsilon_{ij}$ and the electric field vector $E_j$ are defined as (Parton and Kudryavtev, 1988)

$$\varepsilon_{ij} = \frac{1}{2}\left(u_{i,j} + u_{j,i}\right), \quad E_j = -\phi_{,j} \quad (2)$$

where $u_i$ and $\phi$ are displacements and electric potential, respectively.

The strain-gradient tensor $\boldsymbol{\eta}$ is given by

$$\eta_{ijk} = \varepsilon_{ij,k} = \frac{1}{2}\left(u_{i,jk} + u_{j,ik}\right) \tag{3}$$

Under the infinitesimal deformations, the constitutive equations can be obtained from the electric enthalpy density expression (1) (Hu and Shen, 2009; Shen and Hu, 2010)

$$\sigma_{ij} = \frac{\partial H}{\partial \varepsilon_{ij}} = c_{ijkl}\varepsilon_{kl} - e_{kij}E_k - b_{klij}E_{k,l}$$

$$\tau_{jkl} = \frac{\partial H}{\partial \eta_{jkl}} = -f_{ijkl}E_i + g_{jklmni}\eta_{nmi}$$

$$D_i = -\frac{\partial H}{\partial E_i} = a_{ij}E_j + e_{ijk}\varepsilon_{jk} + f_{ijkl}\eta_{jkl}$$

$$Q_{ij} = -\frac{\partial H}{\partial E_{i,j}} = b_{ijkl}\varepsilon_{kl} + h_{ijkl}E_{k,l} \tag{4}$$

Where $\sigma_{ij}$, $D_i$, $\tau_{jkl}$ and $Q_{ij}$ are the stress tensor, electric displacements, higher order stress and electric quadrupole, respectively.

The size scale of higher-order elastic parameters $g_{jklmni}$ is expressed by a proportionality of the conventional elastic stiffness coefficients $c_{klmn}$ and the internal length material parameter $l$ (Gitman et al., 2010; Yaghoubi et al., 2017)

$$g_{jklmni} = l^2 c_{jkmn}\delta_{li} \tag{5}$$

with $\delta_{li}$ being the Kronecker delta.

Similarly, the higher-order electric parameters $\boldsymbol{h}$ is expressed in terms of the dielectric constants $a_{kl}$ and another length-scale parameter $q$ as

$$h_{ijkl} = q^2 a_{ik}\delta_{jl} \tag{6}$$

Deng et al. (2017) considered two independent components $f_1$ and $f_2$ for the direct flexoelectric coefficient $f_{ijkl}$, $f_{ijkl} = f_1\delta_{jk}\delta_{il} + f_2\left(\delta_{ij}\delta_{kl} + \delta_{ik}\delta_{jl}\right)$. Then, the electric enthalpy density has the following form

$$H = \frac{1}{2}c_{ijkl}\varepsilon_{ij}\varepsilon_{kl} - \frac{1}{2}a_{ij}E_iE_j - e_{kji}\varepsilon_{ij}E_k + \frac{l^2}{2}c_{jkmn}\eta_{jkl}\eta_{mnl} - f_1E_i\eta_{kki} - f_2E_i\left(\eta_{ikk} + \eta_{jij}\right) + b_{klij}\varepsilon_{ij}E_{k,l} - \frac{q^2}{2}a_{ik}E_{i,j}E_{k,j} \tag{7}$$

The number of independent converse flexoelectric coefficients $b_{ijkl}$ may be reduced as follows. If in the poling direction is along the $x_3$-axis in the piezoelectric material, the stresses induced by electric intensity vector can be written as

$$\sigma_{11} = e_{31}E_3, \sigma_{33} = e_{33}E_3, \sigma_{13} = e_{15}E_1 \tag{8}$$

with $e_{kij} = \left(e_{31}\delta_{i1}\delta_{j1} + e_{33}\delta_{i3}\delta_{j3}\right)\delta_{k3} + e_{15}\left(\delta_{i1}\delta_{j3} + \delta_{i3}\delta_{j1}\right)\delta_{k1}$, where standard Voight notation is applied for piezoelectric coefficients (Sladek et al., 2018).

Analogously, consider a similar form for induced stresses by the converse flexoelectricity

$$\sigma_{ij} = \delta_{ij}b_1(E_{1,1} + E_{3,3}), \sigma_{13} = \sigma_{31} = b_2E_{1,3} + b_3E_{3,1} \tag{9}$$

with the converse flexoelectric coefficients reduced into three independent coefficients $b_1$, $b_2$ and $b_3$ by $b_{klij} = b_1\delta_{ij}\delta_{kl} + \left(\delta_{i1}\delta_{j3} + \delta_{i3}\delta_{j1}\right)\left(b_2\delta_{k1}\delta_{l3} + b_3\delta_{k3}\delta_{l1}\right)$. With this reduction, the electric enthalpy has the following form

$$H = \frac{1}{2}c_{ijkl}\varepsilon_{ij}\varepsilon_{kl} - \frac{1}{2}a_{ij}E_iE_j - e_{31}\varepsilon_{11}E_3 - e_{33}\varepsilon_{33}E_3 - e_{15}(\varepsilon_{13} + \varepsilon_{31})E_1 + \frac{l^2}{2}c_{jkmn}\eta_{jkl}\eta_{mnl} - f_1E_i\eta_{kki} - f_2E_i\left(\eta_{ikk} + \eta_{jij}\right) + b_1\varepsilon_{kk}E_{i,i} + (b_2E_{1,3} + b_3E_{3,1})(\varepsilon_{13} + \varepsilon_{31}) - \frac{q^2}{2}a_{ik}E_{i,j}E_{k,j} \tag{10}$$

The constitutive Eq. (4) for orthotropic materials ($a_{ij} = a_1\delta_{i1}\delta_{j1} + a_2\delta_{i3}\delta_{j3}$, $c_{ijkl} = \delta_{i1}\delta_{j1}(c_{11}\delta_{k1}\delta_{l1} + c_{13}\delta_{k3}\delta_{l3}) + \delta_{i3}\delta_{j3}(c_{13}\delta_{k1}\delta_{l1} + c_{33}\delta_{k3}\delta_{l3}) + c_{44}\left(\delta_{i1}\delta_{j3} + \delta_{i3}\delta_{j1}\right)\left(\delta_{k1}\delta_{l3} + \delta_{k3}\delta_{l1}\right)$) can be rewritten into a matrix form as (Lekhnitskii, 1963)

$$\begin{bmatrix}\sigma_{11}\\ \sigma_{33}\\ \sigma_{13}\end{bmatrix} = \begin{bmatrix}c_{11} & c_{13} & 0\\ c_{13} & c_{33} & 0\\ 0 & 0 & c_{44}\end{bmatrix}\begin{bmatrix}\varepsilon_{11}\\ \varepsilon_{33}\\ 2\varepsilon_{13}\end{bmatrix} - \begin{bmatrix}0 & e_{31}\\ 0 & e_{33}\\ e_{15} & 0\end{bmatrix}\begin{bmatrix}E_1\\ E_3\end{bmatrix} - \begin{bmatrix}b_1 & 0 & 0 & b_1\\ b_1 & 0 & 0 & b_1\\ 0 & b_3 & b_2 & 0\end{bmatrix}\begin{bmatrix}E_{1,1}\\ E_{3,1}\\ E_{1,3}\\ E_{3,3}\end{bmatrix} =$$

$$= \boldsymbol{C}\begin{bmatrix}\varepsilon_{11}\\ \varepsilon_{33}\\ 2\varepsilon_{13}\end{bmatrix} - \boldsymbol{\Lambda}\begin{bmatrix}E_1\\ E_3\end{bmatrix} - \boldsymbol{\Phi}\begin{bmatrix}E_{1,3}\\ E_{3,3}\end{bmatrix} \tag{11}$$

$$\begin{bmatrix}D_1\\ D_3\end{bmatrix} = \begin{bmatrix}0 & 0 & e_{15}\\ e_{31} & e_{33} & 0\end{bmatrix}\begin{bmatrix}\varepsilon_{11}\\ \varepsilon_{33}\\ 2\varepsilon_{13}\end{bmatrix} + \begin{bmatrix}a_1 & 0\\ 0 & a_2\end{bmatrix}\begin{bmatrix}E_1\\ E_3\end{bmatrix} + \begin{bmatrix}f_1 + 2f_2 & f_1 & 0 & 0 & 0 & f_2\\ 0 & 0 & f_2 & f_1 & f_1 + 2f_2 & 0\end{bmatrix}\begin{bmatrix}\eta_{111}\\ \eta_{331}\\ 2\eta_{131}\\ \eta_{113}\\ \eta_{333}\\ 2\eta_{133}\end{bmatrix} \tag{12}$$

$$== \boldsymbol{\Lambda}^T\begin{bmatrix}\varepsilon_{11}\\ \varepsilon_{33}\\ 2\varepsilon_{13}\end{bmatrix} + \boldsymbol{\Pi}\begin{bmatrix}E_1\\ E_3\end{bmatrix} + \boldsymbol{F}\begin{bmatrix}\eta_{111}\\ \eta_{331}\\ 2\eta_{131}\\ \eta_{113}\\ \eta_{333}\\ 2\eta_{133}\end{bmatrix},$$

$$\begin{bmatrix}\tau_{111}\\ \tau_{331}\\ \tau_{131}\\ \tau_{113}\\ \tau_{333}\\ \tau_{133}\end{bmatrix} = -\begin{bmatrix}f_1 + 2f_2 & 0\\ f_1 & 0\\ 0 & f_2\\ 0 & f_1\\ 0 & f_1 + 2f_2\\ f_2 & 0\end{bmatrix}\begin{bmatrix}E_1\\ E_3\end{bmatrix} + l^2\begin{bmatrix}c_{11} & c_{13} & 0 & 0 & 0 & 0\\ c_{13} & c_{33} & 0 & 0 & 0 & 0\\ 0 & 0 & c_{44} & 0 & 0 & 0\\ 0 & 0 & 0 & c_{11} & c_{13} & 0\\ 0 & 0 & 0 & c_{13} & c_{33} & 0\\ 0 & 0 & 0 & 0 & 0 & c_{44}\end{bmatrix}\begin{bmatrix}\eta_{111}\\ \eta_{331}\\ 2\eta_{131}\\ \eta_{113}\\ \eta_{333}\\ 2\eta_{133}\end{bmatrix} \tag{13}$$

$$== -\boldsymbol{F}^T\begin{bmatrix}E_1\\ E_3\end{bmatrix} + l^2\boldsymbol{G}\begin{bmatrix}\eta_{111}\\ \eta_{331}\\ 2\eta_{131}\\ \eta_{113}\\ \eta_{333}\\ 2\eta_{133}\end{bmatrix}.$$

$$\begin{bmatrix} Q_{11} \\ Q_{31} \\ Q_{13} \\ Q_{33} \end{bmatrix} = \begin{bmatrix} b_1 & b_1 & 0 \\ 0 & 0 & b_3 \\ 0 & 0 & b_2 \\ b_1 & b_1 & 0 \end{bmatrix} \begin{bmatrix} \varepsilon_{11} \\ \varepsilon_{33} \\ 2\varepsilon_{13} \end{bmatrix} + q^2 \begin{bmatrix} a_1 & 0 & 0 & 0 \\ 0 & a_2 & 0 & 0 \\ 0 & 0 & a_1 & 0 \\ 0 & 0 & 0 & a_2 \end{bmatrix} \begin{bmatrix} E_{1,1} \\ E_{3,1} \\ E_{1,3} \\ E_{3,3} \end{bmatrix} = \mathbf{\Phi}^T \begin{bmatrix} \varepsilon_{11} \\ \varepsilon_{33} \\ 2\varepsilon_{13} \end{bmatrix} + q^2 \boldsymbol{H} \begin{bmatrix} E_{1,1} \\ E_{3,1} \\ E_{1,3} \\ E_{3,3} \end{bmatrix} \tag{14}$$

Recently, the authors have derived the governing equations for piezoelectric solid with direct and converse flexoelectric effects (Sladek et al., 2018)

$$\sigma_{ij,j}(\boldsymbol{x}) - \tau_{ijk,jk}(\boldsymbol{x}) = 0$$

$$D_{i,i}(\mathbf{x}) - Q_{ij,ji}(\mathbf{x}) = 0 \tag{15}$$

The essential and natural boundary conditions (b.c.) can be prescribed:

1) Essential b.c.: $u_i(\boldsymbol{x}) = \bar{u}_i(\boldsymbol{x})$on $\Gamma_u$, $\Gamma_u \subset \Gamma$

$$s_i(\mathbf{x}) = \bar{s}_i \text{ on } \Gamma_s, \ \Gamma_s \subset \Gamma \tag{16}$$

$$\phi(\mathbf{x}) = \bar{\phi}(\mathbf{x}) \text{ on } \Gamma_\phi, \ \Gamma_\phi \subset \Gamma$$

$$p(\mathbf{x}) = \frac{\partial \phi}{\partial n} = \bar{p}(\mathbf{x}) \text{ on } \Gamma_p, \ \Gamma_p \subset \Gamma$$

2) Natural b.c.:$t_i(\mathbf{x}) = \bar{t}_i(\mathbf{x})$ on $\Gamma_t \ \Gamma_t \cup \Gamma_u = \Gamma, \ \Gamma_t \cap \Gamma_u = \varnothing$

$$R_i(\mathbf{x}) = \bar{R}_i(\mathbf{x}) \text{ on } \Gamma_R, \ \Gamma_R \cup \Gamma_s = \Gamma, \ \Gamma_R \cap \Gamma_s = \varnothing \tag{17}$$

$$S(\mathbf{x}) = \bar{S}(\mathbf{x}) \text{ on } \Gamma_S, \ \Gamma_S \cup \Gamma_\phi = \Gamma, \ \Gamma_S \cap \Gamma_\phi = \varnothing$$

$$Z(\mathbf{x}) = \bar{Z}(\mathbf{x}) \text{ on } \Gamma_Z, \ \Gamma_Z \cup \Gamma_p = \Gamma, \ \Gamma_Z \cap \Gamma_p = \varnothing$$

Where

$$s_i := \frac{\partial u_i}{\partial n}, \ p := \frac{\partial \phi}{\partial n}, \ R_i := n_k n_j \tau_{ijk}, \ Z := n_i n_j Q_{ij} \tag{18}$$

and the traction vector, and the electric charge are defined as

$$t_i := n_j(\sigma_{ij} - \tau_{ijk,k}) - \frac{\partial \rho_i}{\partial \boldsymbol{\pi}} + \sum_c \| \ \rho_i(\boldsymbol{x}^c) \ \| \delta(\boldsymbol{x} - \boldsymbol{x}^c) \tag{19}$$

$$S := n_k(D_k - Q_{kjj}) - \frac{\partial \alpha}{\partial \boldsymbol{\pi}} + \sum_c \| \ \alpha(\mathbf{x}^c) \ \| \delta(\mathbf{x} - \mathbf{x}^c) \tag{20}$$

with $\rho_i := n_k \pi_j \tau_{ijk}, \alpha := n_i \pi_j Q_{ij}$, $\delta(\mathbf{x})$ being the Dirac delta function and $\pi_i$ is the Cartesian component of the unit tangent vector on $\Gamma$.

The jump at a corner ($\mathbf{x}^c$) on the oriented boundary contour $\Gamma$ is defined as

$$\| \ \rho_i(\mathbf{x}^c) \ \| := \rho_i(\mathbf{x}^c + 0) - \rho_i(\mathbf{x}^c - 0) \tag{21}$$

$$\| \ \alpha(\mathbf{x}^c) \ \| := \alpha(\mathbf{x}^c + 0) - \alpha(\mathbf{x}^c - 0) \tag{22}$$

## 3. The mixed finite element using collocation method

To solve the strain- and electric intensity vector-gradient effects in flexoelectric materials, a collocation MFEM is developed. In the present scheme, the displacements and strains are set as independent variables with $C^0$ continuity. However, the strains should also satisfy the geometric relationship with the displacements. To this end, the strain values from these two considerations are made to be equal at the Gauss points in the elements (Dong and Atluri, 2011; Bishay et al., 2012). The kinematic constraints between strains and displacements are thus satisfied by the collocation method at Gauss points. This is similarly applied to the electric potential and electric intensity vector. By using this collocation scheme, each node has only three DOFs (two displacements and one electric potential) which is significantly smaller in number as compared to the traditional MFEM via Lagrangian multipliers (Mao et al., 2016; Deng et al., 2017).

The variational formulation of the FEM in gradient theory can be derived from the principle of virtual work as (Hu and Shen 2009)

$$\int_V \left(\sigma_{ij}\delta\varepsilon_{ij} + \tau_{ijk}\delta\eta_{ijk} + D_k\delta E_k + Q_{ij}\delta E_{i,j}\right) d\Omega = \int_{\Gamma_t} \bar{t}_i \delta u_i d\Gamma + \int_{\Gamma_R} \bar{R}_i \delta s_i d\Gamma + \int_{\Gamma_S} \bar{S}\,\delta\phi d\Gamma + \int_{\Gamma_Z} \bar{Z}\,\delta p d\Gamma \tag{23}$$

Where $\bar{t}_i$, $\bar{R}_i$, $\bar{S}$, and $\bar{Z}$ are prescribed values corresponding to the external work on the right hand side of (23).

The mechnanical displacements and electric potential in each element as shown in Fig. 1 are expressed in terms of nodal values and shape functions

$$\left.\begin{pmatrix} u_1(\boldsymbol{x}) \\ u_3(\boldsymbol{x}) \end{pmatrix}\right|_{V^e} = \sum_{a=1}^4 \begin{pmatrix} u_1^{(ea)} \\ u_3^{(ea)} \end{pmatrix} N^a(\xi_1, \xi_2) = \sum_{a=1}^4 \{q^{(ea)}\} N^a(\xi_1, \xi_2), \{q^{(ea)}\} := \begin{pmatrix} u_1^{(ea)} \\ u_3^{(ea)} \end{pmatrix}$$
$$\phi(\boldsymbol{x})|_{V^e} = \sum_{a=1}^4 \phi^{(ea)} N^a(\xi_1, \xi_2) \tag{24}$$

where $\{q^{(ea)}\}$ and $\phi^{(ea)}$ are nodal displacements and electric potential, respectively.

The gradient in global coordinates can be expressed within the finite element $V^e$ in terms of deivatives in the local (intrinsic) coordinates as

$$\left.\begin{pmatrix} \partial/\partial x_1 \\ \partial/\partial x_3 \end{pmatrix}\right|_{V^e} = [Y^e] \begin{pmatrix} \partial/\partial \xi_1 \\ \partial/\partial \xi_2 \end{pmatrix}, [Y^e] = [J^e]^{-1}$$

$$[J^e] = \left.\begin{pmatrix} \partial x_1/\partial \xi_1 & \partial x_3/\partial \xi_1 \\ \partial x_1/\partial \xi_2 & \partial x_3/\partial \xi_2 \end{pmatrix}\right|_{V^e} = \sum_c \begin{pmatrix} x_1^{(ec)} N_{,1}^c & x_3^{(ec)} N_{,1}^c \\ x_1^{(ec)} N_{,2}^c & x_3^{(ec)} N_{,2}^c \end{pmatrix} \tag{25}$$

Hence

$$\left.\frac{\partial f}{\partial x_i}\right|_{V^e} = \sum_a f^{(ea)} b_i^{ea}(\xi_1, \xi_2),$$
$$b_1^{ea}(\boldsymbol{\xi}) = Y_{11}^e(\boldsymbol{\xi}) N_{,1}^a(\boldsymbol{\xi}) + Y_{12}^e(\boldsymbol{\xi}) N_{,2}^a(\boldsymbol{\xi}),$$
$$b_3^{ea}(\boldsymbol{\xi}) = Y_{21}^e(\boldsymbol{\xi}) N_{,1}^a(\boldsymbol{\xi}) + Y_{22}^e(\boldsymbol{\xi}) N_{,2}^a(\boldsymbol{\xi}) \tag{26}$$

The expression for the approximation of the electric intensity vector within $V^e$, from the Maxwell equation, is given by

$$\{-\boldsymbol{E}\}|_{V^e} = -\left.\begin{pmatrix} E_1 \\ E_3 \end{pmatrix}\right|_{V^e} = \left.\begin{pmatrix} \phi_{,1} \\ \phi_{,3} \end{pmatrix}\right|_{V^e} = \sum_a \left\{B_\phi^{ea}(\boldsymbol{\xi})\right\} \phi^{(ea)} \left\{B_\phi^{ea}(\boldsymbol{\xi})\right\} = \begin{pmatrix} b_1^{ea}(\boldsymbol{\xi}) \\ b_3^{ea}(\boldsymbol{\xi}) \end{pmatrix} \tag{27}$$

The electric intensity vector is treated as independent variable; thus,

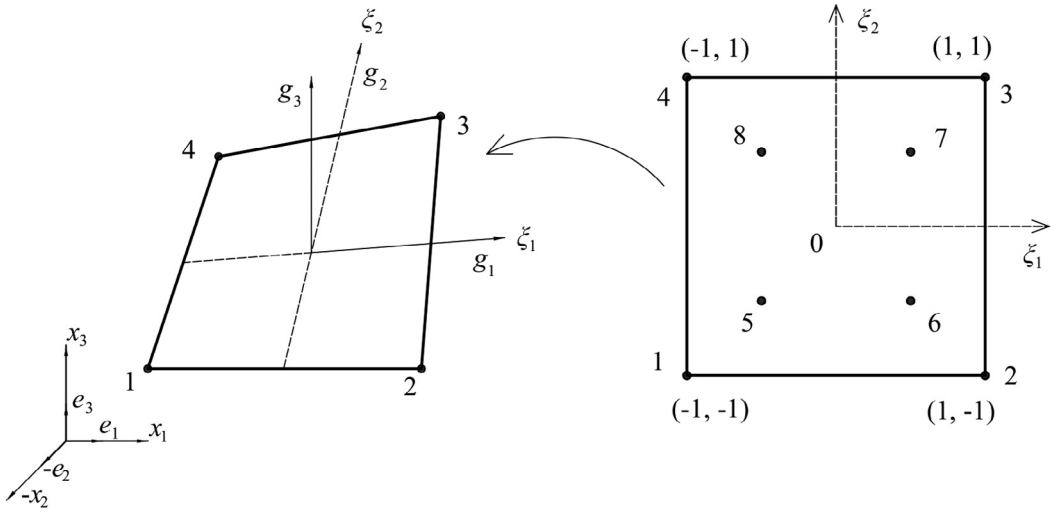


**Fig. 1.** Global Cartesian coordinates $x_1 - x_2 - x_3$, curvilinear coordinates $\xi_1 - \xi_2$, for the 4-node quadrilateral finite element.

$$-E_i^{In}(\boldsymbol{x})\Big|_{V^e} = \underbrace{(\,1 \quad \xi_1 \quad \xi_2 \quad \xi_1\xi_2\,)}_{\{P(\xi)\}^T}\begin{pmatrix}\beta_i^1\\ \beta_i^2\\ \beta_i^3\\ \beta_i^4\end{pmatrix} = \{P(\xi)\}^T\begin{pmatrix}\beta_i^1\\ \beta_i^2\\ \beta_i^3\\ \beta_i^4\end{pmatrix} \tag{28}$$

or

$$-\left\{E^{In}(\boldsymbol{x})\right\}^T\Big|_{V^e} = -\left(E_1^{In}(\boldsymbol{x}) \quad E_3^{In}(\boldsymbol{x})\right)\Big|_{V^e}$$
$$= (\,1 \quad \xi_1 \quad \xi_2 \quad \xi_1\xi_2\,)\begin{pmatrix}\beta_1^1 & \beta_3^1\\ \beta_1^2 & \beta_3^2\\ \beta_1^3 & \beta_3^3\\ \beta_1^4 & \beta_3^4\end{pmatrix} \tag{29}$$

with the coefficients $\beta_i^c$ being determined from equating the two approximations at collocation points $\boldsymbol{x}^c$, selected as the Gauss points, in the element $V^e$ with intrinsic coordinates $(\xi_1^c,\ \xi_2^c)$, i.e. $E_i^{In}(\boldsymbol{x}^c) = E_i(\boldsymbol{x}^c)$. Thus,

$$-\begin{pmatrix}E_i^{In}(\boldsymbol{x}^1)\\ E_i^{In}(\boldsymbol{x}^2)\\ E_i^{In}(\boldsymbol{x}^3)\\ E_i^{In}(\boldsymbol{x}^4)\end{pmatrix}\Bigg|_{V^e} = \underbrace{\begin{pmatrix}1 & \xi_1^1 & \xi_2^1 & \xi_1^1\xi_2^1\\ 1 & \xi_1^2 & \xi_2^2 & \xi_1^2\xi_2^2\\ 1 & \xi_1^3 & \xi_2^3 & \xi_1^3\xi_2^3\\ 1 & \xi_1^4 & \xi_1^4 & \xi_1^4\xi_2^4\end{pmatrix}}_{[A]}\begin{pmatrix}\beta_i^1\\ \beta_i^2\\ \beta_i^3\\ \beta_i^4\end{pmatrix}$$
$$= -\begin{pmatrix}E_i(\boldsymbol{x}^1)\\ E_i(\boldsymbol{x}^2)\\ E_i(\boldsymbol{x}^3)\\ E_i(\boldsymbol{x}^4)\end{pmatrix}\Bigg|_{V^e} = \sum_a \begin{pmatrix}B_{\phi i}^{ea}(\xi^1)\\ B_{\phi i}^{ea}(\xi^2)\\ B_{\phi i}^{ea}(\xi^3)\\ B_{\phi i}^{ea}(\xi^4)\end{pmatrix}\phi^{(ea)},\quad B_{\phi i}^{ea}(\xi^c) = b_i^{ea}(\xi^c), \tag{30}$$

Hence,

$$\{\beta_i\} := \begin{pmatrix}\beta_i^1\\ \beta_i^2\\ \beta_i^3\\ \beta_i^4\end{pmatrix} = [A]^{-1}\sum_a \begin{pmatrix}b_i^{ea}(\xi^1)\\ b_i^{ea}(\xi^2)\\ b_i^{ea}(\xi^3)\\ b_i^{ea}(\xi^4)\end{pmatrix}\phi^{(ea)}$$
$$= [A]^{-1}\sum_a \{\omega_i^{ea}\}\phi^{(ea)}, \{\omega_i^{ea}\} := \begin{pmatrix}b_i^{ea}(\xi^1)\\ b_i^{ea}(\xi^2)\\ b_i^{ea}(\xi^3)\\ b_i^{ea}(\xi^4)\end{pmatrix} \tag{31}$$

Substituting Eqs. (31) into (28), one can obtain

$$-E_i^{In}(\boldsymbol{x})\Big|_{V^e} = \{L(\xi)\}^T\sum_a \{\omega_i^{ea}\}\phi^{(ea)}, \{L(\xi)\}^T := \{P(\xi)\}^T[A]^{-1} \tag{32}$$

or

$$-\left\{E^{In}(\boldsymbol{x})\right\}\Big|_{V^e} = -\begin{pmatrix}E_1^{In}(\boldsymbol{x})\\ E_3^{In}(\boldsymbol{x})\end{pmatrix}\Bigg|_{V^e} = \sum_a \begin{pmatrix}\{L(\xi)\}^T\{\omega_1^{ea}\}\\ \{L(\xi)\}^T\{\omega_3^{ea}\}\end{pmatrix}\phi^{(ea)}$$
$$= \sum_a \begin{pmatrix}v_1^{ea}(\xi)\\ v_3^{ea}(\xi)\end{pmatrix}\phi^{(ea)}$$

$$v_i^{ea}(\xi) := \{L(\xi)\}^T\{\omega_i^{ea}\} = \sum_c \{L(\xi)\}_c b_i^{ea}(\xi^c) \tag{33}$$

and

$$-\left\{E^{In}(\boldsymbol{x})\right\}^T\Big|_{V^e} = -\left(E_1^{In}(\boldsymbol{x}) \quad E_3^{In}(\boldsymbol{x})\right)\Big|_{V^e} = \sum_a \left(v_1^{ea}(\xi) \quad v_3^{ea}(\xi)\right)\phi^{(ea)} \tag{34}$$

Since $\frac{\partial}{\partial x_1}\Big|_{V^e} = Y_{11}^e\frac{\partial}{\partial\xi_1} + Y_{12}^e\frac{\partial}{\partial\xi_2}, \frac{\partial}{\partial x_3}\Big|_{V^e} = Y_{21}^e\frac{\partial}{\partial\xi_1} + Y_{22}^e\frac{\partial}{\partial\xi_2}$, the electric intensity vector gradient can be derived as

$$-\frac{\partial E_i^{In}(\boldsymbol{x})}{\partial x_1}\Big|_{V^e} = \underbrace{\left(Y_{11}^e\frac{\partial}{\partial\xi_1} + Y_{12}^e\frac{\partial}{\partial\xi_2}\right)\{P(\xi)\}^T}_{\{P_1(\xi)\}^T}\{\beta_i\}$$
$$= \{S_1(\xi)\}^T\sum_a \{\omega_i^{ea}\}\phi^{(ea)}$$

$$-\frac{\partial E_i^{In}(\boldsymbol{x})}{\partial x_3}\Big|_{V^e} = \underbrace{\left(Y_{21}^e\frac{\partial}{\partial\xi_1} + Y_{22}^e\frac{\partial}{\partial\xi_2}\right)\{P(\xi)\}^T}_{\{P_3(\xi)\}^T}\{\beta_i\}$$
$$= \{S_3(\xi)\}^T\sum_a \{\omega_i^{ea}\}\phi^{(ea)}$$

$$\{S_j(\xi)\}^T := \{P_j(\xi)\}^T[A]^{-1} \tag{35}$$

or

$$-E_{ij}^{In}(\boldsymbol{x})\Big|_{V^e} = \sum_a \mu_{ij}^{ea}(\xi)\phi^{(ea)}, \mu_{ij}^{ea}(\xi) := \sum_c \{S_j(\xi)\}_c b_i^{ea}(\xi^c) \tag{36}$$

and its matrix form is

$$-\left.\begin{pmatrix}\left\{E^{ln}(\boldsymbol{x})\right\}_{,1}\\ \left\{E^{ln}(\boldsymbol{x})\right\}_{,3}\end{pmatrix}\right|_{V^e}=-\left.\begin{pmatrix}E^{ln}_{1,1}(\boldsymbol{x})\\ E^{ln}_{3,1}(\boldsymbol{x})\\ E^{ln}_{1,3}(\boldsymbol{x})\\ E^{ln}_{3,3}(\boldsymbol{x})\end{pmatrix}\right|_{V^e}=\sum_a\begin{pmatrix}\mu^{ea}_{11}(\xi)\\ \mu^{ea}_{31}(\xi)\\ \mu^{ea}_{13}(\xi)\\ \mu^{ea}_{33}(\xi)\end{pmatrix}\phi^{(ea)} \tag{37}$$

A similar derivation can be repeated for the approximation of the strain tensor. The expression for the strain tensor obtained from the geometric relationship within $V^e$ is given by

$$\{\boldsymbol{\varepsilon}\}|_{V^e}=\sum_a\left[B^{ea}_{\varepsilon}(\xi)\right]\{q^{(ea)}_u\},\left[B^{ea}_{\varepsilon}(\xi)\right]=\begin{pmatrix}b^{ea}_1(\xi) & 0\\ 0 & b^{ea}_3(\xi)\\ \frac{1}{2}b^{ea}_3(\xi) & \frac{1}{2}b^{ea}_1(\xi)\end{pmatrix},\quad \{q^{(ea)}_u\}=\begin{pmatrix}u^{(ea)}_1\\ u^{(ea)}_3\end{pmatrix} \tag{38}$$

The strain tensor is also set as independent variable; thus,

$$\hat{\varepsilon}^{ln}_{ij}(\boldsymbol{x})\Big|_{V^e}=\begin{pmatrix}1 & \xi_1 & \xi_2 & \xi_1\xi_2\end{pmatrix}\begin{pmatrix}\alpha^1_{ij}\\ \alpha^2_{ij}\\ \alpha^3_{ij}\\ \alpha^4_{ij}\end{pmatrix}=\{P(\xi)\}^T\begin{pmatrix}\alpha^1_{ij}\\ \alpha^2_{ij}\\ \alpha^3_{ij}\\ \alpha^4_{ij}\end{pmatrix},\quad \hat{\varepsilon}^{ln}_{ij}:=\begin{cases}\varepsilon^{ln}_{ij}, & \text{if } i=j\\ 2\varepsilon^{ln}_{ij}, & \text{if } i\neq j\end{cases} \tag{39}$$

or

$$\begin{aligned}&\left\{\varepsilon^{ln}_{11}(\boldsymbol{x})\quad \varepsilon^{ln}_{33}(\boldsymbol{x})\quad 2\varepsilon^{ln}_{13}(\boldsymbol{x})\right\}|_{V^e}\\ &=\begin{pmatrix}1 & \xi_1 & \xi_2 & \xi_1\xi_2\end{pmatrix}\begin{pmatrix}\alpha^1_{11} & \alpha^1_{33} & \alpha^1_{13}\\ \alpha^2_{11} & \alpha^2_{33} & \alpha^2_{13}\\ \alpha^3_{11} & \alpha^3_{33} & \alpha^3_{13}\\ \alpha^4_{11} & \alpha^4_{33} & \alpha^4_{13}\end{pmatrix}\end{aligned} \tag{40}$$

where the coefficents $\alpha^c_{ij}(c=1,2,3,4)$ are determined from the collocation of $\hat{\varepsilon}^{ln}_{ij}(\boldsymbol{x}^c)=\hat{\varepsilon}_{ij}(\boldsymbol{x}^c)$ at the Gauss points $\boldsymbol{x}^c$ in the finite element $V^e$ with

$$\hat{\varepsilon}_{ij}:=\begin{cases}\varepsilon_{ij}, & \text{if } i=j\\ 2\varepsilon_{ij}, & \text{if } i\neq j\end{cases},\hat{\varepsilon}_{ij}(\boldsymbol{x}^c)|_{V^e}=\sum_a\left\{B^{ea}_{\varepsilon ij}(\xi^c)\right\}^T\{q^{(ea)}_u\} \tag{41}$$

where

$$\begin{aligned}&\left\{B^{ea}_{\varepsilon 11}(\xi^c)\right\}^T=\begin{pmatrix}b^{ea}_1(\xi^c) & 0\end{pmatrix},\\ &\left\{B^{ea}_{\varepsilon 33}(\xi^c)\right\}^T=\begin{pmatrix}0 & b^{ea}_3(\xi^c)\end{pmatrix},\left\{B^{ea}_{\varepsilon 13}(\xi^c)\right\}^T=\begin{pmatrix}b^{ea}_3(\xi^c) & b^{ea}_1(\xi^c)\end{pmatrix}\end{aligned} \tag{42}$$

Thus,

$$\begin{aligned}\left.\begin{pmatrix}\hat{\varepsilon}^{ln}_{ij}(\boldsymbol{x}^1)\\ \hat{\varepsilon}^{ln}_{ij}(\boldsymbol{x}^2)\\ \hat{\varepsilon}^{ln}_{ij}(\boldsymbol{x}^3)\\ \hat{\varepsilon}^{ln}_{ij}(\boldsymbol{x}^4)\end{pmatrix}\right|_{V^e}&=\underbrace{\begin{pmatrix}1 & \xi^1_1 & \xi^1_2 & \xi^1_1\xi^1_2\\ 1 & \xi^2_1 & \xi^2_2 & \xi^2_1\xi^2_2\\ 1 & \xi^3_1 & \xi^3_2 & \xi^3_1\xi^3_2\\ 1 & \xi^4_1 & \xi^4_2 & \xi^4_1\xi^4_2\end{pmatrix}}_{[A]}\begin{pmatrix}\alpha^1_{ij}\\ \alpha^2_{ij}\\ \alpha^3_{ij}\\ \alpha^4_{ij}\end{pmatrix}\\ =\sum_a\begin{pmatrix}\left\{B^{ea}_{\varepsilon ij}(\xi^1)\right\}^T\\ \left\{B^{ea}_{\varepsilon ij}(\xi^2)\right\}^T\\ \left\{B^{ea}_{\varepsilon ij}(\xi^3)\right\}^T\\ \left\{B^{ea}_{\varepsilon ij}(\xi^4)\right\}^T\end{pmatrix}\{q^{(ea)}_u\}&=\left.\begin{pmatrix}\hat{\varepsilon}_{ij}(\boldsymbol{x}^1)\\ \hat{\varepsilon}_{ij}(\boldsymbol{x}^2)\\ \hat{\varepsilon}_{ij}(\boldsymbol{x}^3)\\ \hat{\varepsilon}_{ij}(\boldsymbol{x}^4)\end{pmatrix}\right|_{V^e}\end{aligned} \tag{43}$$

Hence

$$\{\alpha_{ij}\}:=\begin{pmatrix}\alpha^1_{ij}\\ \alpha^2_{ij}\\ \alpha^3_{ij}\\ \alpha^4_{ij}\end{pmatrix}=[A]^{-1}\sum_a\begin{pmatrix}\left\{B^{ea}_{\varepsilon ij}(\xi^1)\right\}^T\\ \left\{B^{ea}_{\varepsilon ij}(\xi^2)\right\}^T\\ \left\{B^{ea}_{\varepsilon ij}(\xi^3)\right\}^T\\ \left\{B^{ea}_{\varepsilon ij}(\xi^4)\right\}^T\end{pmatrix} \tag{44}$$

$$\{q^{(ea)}_u\}=[A]^{-1}\sum_a\begin{pmatrix}\left\{B^{ea}_{\varepsilon ij}(\xi^1)\right\}^T\{q^{(ea)}_u\}\\ \left\{B^{ea}_{\varepsilon ij}(\xi^2)\right\}^T\{q^{(ea)}_u\}\\ \left\{B^{ea}_{\varepsilon ij}(\xi^3)\right\}^T\{q^{(ea)}_u\}\\ \left\{B^{ea}_{\varepsilon ij}(\xi^4)\right\}^T\{q^{(ea)}_u\}\end{pmatrix}=[A]^{-1}\sum_a\left\{\gamma^{ea}_{ij}\right\}$$

in which

$$\left\{\gamma^{ea}_{ij}\right\}:=\begin{pmatrix}\left\{B^{ea}_{\varepsilon ij}(\xi^1)\right\}^T\{q^{(ea)}_u\}\\ \left\{B^{ea}_{\varepsilon ij}(\xi^2)\right\}^T\{q^{(ea)}_u\}\\ \left\{B^{ea}_{\varepsilon ij}(\xi^3)\right\}^T\{q^{(ea)}_u\}\\ \left\{B^{ea}_{\varepsilon ij}(\xi^4)\right\}^T\{q^{(ea)}_u\}\end{pmatrix} \tag{45}$$

Then,

$$\hat{\varepsilon}^{ln}_{ij}(\boldsymbol{x})\Big|_{V^e}=\{P(\xi)\}^T\begin{pmatrix}\alpha^1_{ij}\\ \alpha^2_{ij}\\ \alpha^3_{ij}\\ \alpha^4_{ij}\end{pmatrix}=\underbrace{\{P(\xi)\}^T[A]^{-1}}_{\{L(\xi)\}^T}\sum_a\left\{\gamma^{ea}_{ij}\right\}=\{L(\xi)\}^T\sum_a\left\{\gamma^{ea}_{ij}\right\} \tag{46}$$

or

$$\left\{\hat{\varepsilon}^{ln}(\boldsymbol{x})\right\}\Big|_{V^e}=\left.\begin{pmatrix}\varepsilon^{ln}_{11}(\boldsymbol{x})\\ \varepsilon^{ln}_{33}(\boldsymbol{x})\\ 2\varepsilon^{ln}_{13}(\boldsymbol{x})\end{pmatrix}\right|_{V^e}=\sum_a\begin{pmatrix}\{L(\xi)\}^T\{\gamma^{ea}_{11}\}\\ \{L(\xi)\}^T\{\gamma^{ea}_{33}\}\\ \{L(\xi)\}^T\{\gamma^{ea}_{13}\}\end{pmatrix} \tag{47}$$

Since

$$\{L(\xi)\}^T\left\{\gamma^{ea}_{ij}\right\}=\left(\{L(\xi)\}^T\left\{\beta^{ea}_{ij}\right\}\right)\{q^{(ea)}_u\},\left\{\beta^{ea}_{ij}\right\}:=\begin{pmatrix}\left\{B^{ea}_{\varepsilon ij}(\xi^1)\right\}^T\\ \left\{B^{ea}_{\varepsilon ij}(\xi^2)\right\}^T\\ \left\{B^{ea}_{\varepsilon ij}(\xi^3)\right\}^T\\ \left\{B^{ea}_{\varepsilon ij}(\xi^4)\right\}^T\end{pmatrix} \tag{48}$$

The following is finally obtained,

$$\begin{aligned}\{\varepsilon^{ln}(\boldsymbol{x})\}|_{V^e}&=\left.\begin{pmatrix}\hat{\varepsilon}^{ln}_{11}(\boldsymbol{x})\\ \hat{\varepsilon}^{ln}_{33}(\boldsymbol{x})\\ 2\hat{\varepsilon}^{ln}_{13}(\boldsymbol{x})\end{pmatrix}\right|_{V^e}=\sum_a\begin{pmatrix}\{L(\xi)\}^T\{\beta^{ea}_{11}\}\\ \{L(\xi)\}^T\{\beta^{ea}_{33}\}\\ \{L(\xi)\}^T\{\beta^{ea}_{13}\}\end{pmatrix}\\ \{q^{(ea)}_u\}&=\sum_a\begin{pmatrix}\{\mathrm{M}^{ea}_{11}(\xi)\}^T\\ \{\mathrm{M}^{ea}_{33}(\xi)\}^T\\ \{\mathrm{M}^{ea}_{13}(\xi)\}^T\end{pmatrix}\{q^{(ea)}_u\}=\sum_a\left[\mathrm{M}^{ea}\right]\{q^{(ea)}_u\}\end{aligned} \tag{49}$$

where

$$\begin{aligned}\{\mathrm{M}^{ea}_{11}(\xi)\}^T&:=\{L(\xi)\}^T\{\beta^{ea}_{11}\}=\begin{pmatrix}\lambda^{ea}_1(\xi) & 0\end{pmatrix}\\ \{\mathrm{M}^{ea}_{33}(\xi)\}^T&:=\{L(\xi)\}^T\{\beta^{ea}_{33}\}=\begin{pmatrix}0 & \lambda^{ea}_3(\xi)\end{pmatrix}\\ \{\mathrm{M}^{ea}_{13}(\xi)\}^T&:=\{L(\xi)\}^T\{\beta^{ea}_{13}\}=\begin{pmatrix}\lambda^{ea}_3(\xi) & \lambda^{ea}_1(\xi)\end{pmatrix}\end{aligned} \tag{50}$$

and

$$\lambda_1^{ea}(\xi) := \sum_{c=1}^{4} \{L(\xi)\}_c b_1^{ea}(\xi^c), \lambda_3^{ea}(\xi) := \sum_{c=1}^{4} \{L(\xi)\}_c b_3^{ea}(\xi^c) \tag{51}$$

Thus,

$$\begin{aligned} &\left\{\hat{\varepsilon}^{In}(\boldsymbol{x})\right\}^T\Big|_{V^e} = \left(\varepsilon_{11}^{In}(\boldsymbol{x}) \quad \varepsilon_{33}^{In}(\boldsymbol{x}) \quad 2\varepsilon_{13}^{In}(\boldsymbol{x})\right)\Big|_{V^e} \\ &= \sum_a \left\{q_u^{(ea)}\right\}^T \left(\left\{\mathrm{M}_{11}^{ea}(\xi)\right\} \quad \left\{\mathrm{M}_{33}^{ea}(\xi)\right\} \quad \left\{\mathrm{M}_{13}^{ea}(\xi)\right\}\right) \end{aligned} \tag{52}$$

with

$$\begin{aligned} &\left\{q_u^{(ea)}\right\}^T = \begin{pmatrix} u_1^{(ea)} & u_3^{(ea)} \end{pmatrix}, \left\{\mathrm{M}_{11}^{ea}(\xi)\right\} = \begin{pmatrix} \lambda_1^{ea}(\xi) \\ 0 \end{pmatrix}, \\ &\left\{\mathrm{M}_{33}^{ea}(\xi)\right\} = \begin{pmatrix} 0 \\ \lambda_3^{ea}(\xi) \end{pmatrix}, \left\{\mathrm{M}_{13}^{ea}(\xi)\right\} = \begin{pmatrix} \lambda_3^{ea}(\xi) \\ \lambda_1^{ea}(\xi) \end{pmatrix} \end{aligned} \tag{53}$$

For derivatives of strains, the approximation of these gradients can be written as

$$\begin{aligned} \hat{\varepsilon}_{ij,k}^{In}(\boldsymbol{x})\Big|_{V^e} &= \{P_k(\xi)\}^T\{\alpha_{ij}\} = \{P_k(\xi)\}^T[A]^{-1}\sum_a \left\{\gamma_{ij}^{ea}\right\} \\ &= \{S_k(\xi)\}^T \sum_a \left\{\gamma_{ij}^{ea}\right\} \end{aligned} \tag{54}$$

Since

$$\{S_k(\xi)\}^T\left\{\gamma_{ij}^{ea}\right\} = \left(\{S_k(\xi)\}^T\left\{\beta_{ij}^{ea}\right\}\right)\left\{q_u^{(ea)}\right\} = \left\{\Omega_{ijk}^{ea}(\xi)\right\}^T\left\{q_u^{(ea)}\right\} \tag{55}$$

with

$$\begin{aligned} &\left\{\Omega_{111}^{ea}(\xi)\right\}^T := \begin{pmatrix} \chi_1^{ea}(\xi) & 0 \end{pmatrix} \left\{\Omega_{331}^{ea}(\xi)\right\}^T := \begin{pmatrix} 0 & \chi_3^{ea}(\xi) \end{pmatrix} \\ &\left\{\Omega_{131}^{ea}(\xi)\right\}^T := \begin{pmatrix} \chi_3^{ea}(\xi) & \chi_1^{ea}(\xi) \end{pmatrix} \\ &\left\{\Omega_{113}^{ea}(\xi)\right\}^T := \begin{pmatrix} \kappa_1^{ea}(\xi) & 0 \end{pmatrix} \left\{\Omega_{333}^{ea}(\xi)\right\}^T := \begin{pmatrix} 0 & \kappa_3^{ea}(\xi) \end{pmatrix} \\ &\left\{\Omega_{133}^{ea}(\xi)\right\}^T := \begin{pmatrix} \kappa_3^{ea}(\xi) & \kappa_1^{ea}(\xi) \end{pmatrix} \end{aligned}$$

$$\chi_j^{ea}(\xi) := \sum_c \{S_1(\xi)\}_c b_j^{ea}(\xi^c), \kappa_j^{ea}(\xi) := \sum_c \{S_3(\xi)\}_c b_j^{ea}(\xi^c) \tag{56}$$

this yields

$$\begin{aligned} \left\{\eta^{In}(\boldsymbol{x})\right\}\Big|_{V^e} &= \begin{pmatrix} \left\{\hat{\varepsilon}^{In}(\boldsymbol{x})\right\}_{,1} \\ \left\{\hat{\varepsilon}^{In}(\boldsymbol{x})\right\}_{,3} \end{pmatrix}\Bigg|_{V^e} = \sum_a \begin{pmatrix} \left(\chi_1^{ea}(\xi) \quad 0\right) \\ \left(0 \quad \chi_3^{ea}(\xi)\right) \\ \left(\chi_3^{ea}(\xi) \quad \chi_1^{ea}(\xi)\right) \\ \left(\kappa_1^{ea}(\xi) \quad 0\right) \\ \left(0 \quad \kappa_3^{ea}(\xi)\right) \\ \left(\kappa_3^{ea}(\xi) \quad \kappa_1^{ea}(\xi)\right) \end{pmatrix} \\ \left\{q_u^{(ea)}\right\} &= \sum_a \left[\Psi^{ea}\right]\left\{q_u^{(ea)}\right\} \end{aligned} \tag{57}$$

The above approximations further results in the following expression being obtained,

$$\sigma_{ij}\delta\varepsilon_{ij}\Big|_{V^e} = \sum_{c,a}\left\{\delta q_u^{(ec)}\right\}^T\left[M^{ec}(\xi)\right]^T\left([\mathbf{C}]\left[M^{ea}(\xi)\right]\left\{q_u^{(ea)}\right\} - \left([\Lambda]\{v^{ea}(\xi)\} + [\Phi]\{\mu^{ea}(\xi)\}\right)\phi^{(ea)}\right)$$

$$\tau_{ijk}\delta\eta_{ijk}\Big|_{V^e} = \sum_{c,a}\left\{\delta q_u^{(ec)}\right\}^T\left[\Psi^{ec}(\xi)\right]^T\left(-[\mathbf{F}]^T\{v^{ea}(\xi)\}\phi^{(ea)} + l^2[\mathbf{G}]\left[\Psi^{ea}(\xi)\right]\left\{q_u^{(ea)}\right\}\right)$$

$$D_k\delta E_k|_{V^e} = \sum_{c,a}\delta\phi^{(ec)}\{v^{ec}(\xi)\}^T\left([\Pi]^T\{v^{ea}(\xi)\}\phi^{(ea)} + \left([\Lambda]\left[\mathrm{M}^{ea}(\xi)\right] + [\mathbf{F}]\left[\Psi^{ea}(\xi)\right]\right)\left\{q_u^{(ea)}\right\}\right)$$

$$Q_{ij}\delta E_{ij}\Big|_{V^e} = \sum_{c,a}\delta\phi^{(ec)}\{\mu^{ec}(\xi)\}^T\left([\Phi]^T\left[\mathrm{M}^{ea}(\xi)\right]\left\{q_u^{(ea)}\right\} + q^2[\mathbf{H}]\{\mu^{ea}(\xi)\}\phi^{(ea)}\right) \tag{58}$$

and the variational condition (23) becomes

$$\begin{aligned} &\sum_e\sum_{c,a}\int_{V^e}\left\{\delta q_u^{(ec)}\right\}^T\left\{\left([M^{ec}(\xi)]^T[\mathbf{C}]\left[M^{ea}(\xi)\right] + l^2\left[\Psi^{ec}(\xi)\right]^T[\mathbf{G}]\left[\Psi^{ea}(\xi)\right]\right)\left\{q_u^{(ea)}\right\}\right. \\ &\left.-\left([M^{ec}(\xi)]^T([\Lambda]\{v^{ea}(\xi)\} + [\Phi]\{\mu^{ea}(\xi)\}) + \left[\Psi^{ec}(\xi)\right]^T[\mathbf{F}]^T\{v^{ea}(\xi)\}\right)\phi^{(ea)}\right\}dV \\ &+\sum_e\sum_{c,a}\int_{V^e}\delta\phi^{(ec)}\left\{\left(\{v^{ec}(\xi)\}^T([\Lambda]\left[\mathrm{M}^{ea}(\xi)\right] + [\mathbf{F}]\left[\Psi^{ea}(\xi)\right]\right)\right. \\ &\left.+\{\mu^{ec}(\xi)\}^T[\Phi]^T\left[\mathrm{M}^{ea}(\xi)\right]\right)\left\{q_u^{(ea)}\right\} \\ &+\left(\{v^{ec}(\xi)\}^T[\Pi]^T\{v^{ea}(\xi)\} + q^2\{\mu^{ec}(\xi)\}^T[\mathbf{H}]\{\mu^{ea}(\xi)\}\right)\phi^{(ea)}\Big\}dV \\ &=\sum_e\sum_c\left[\left\{\delta q_u^{(ec)}\right\}^T\left(\int_{\Gamma_t^e}\{T(\xi)\}N^c(\xi)d\Gamma + \int_{\Gamma_R^e}\{R(\xi)\}n_j(\xi)b_j^{ec}(\xi)d\Gamma\right)\right. \\ &\left.+\delta\phi^{(ec)}\left(\int_{\Gamma_S^e}\bar{S}(\xi)N^c(\xi)d\Gamma + \int_{\Gamma_Z^e}\bar{Z}(\xi)n_j(\xi)b_j^{ec}(\xi)d\Gamma\right),\right. \end{aligned} \tag{59}$$

where $\Gamma_t^e = V^e \cap \Gamma_t$, $\Gamma_R^e = V^e \cap \Gamma_R$, $\Gamma_S^e = V^e \cap \Gamma_S$, $\Gamma_Z^e = V^e \cap \Gamma_Z$, $\Gamma^e = \partial V \cap V^e$, $\{T\} = \begin{pmatrix} \bar{t}_1 \\ \bar{t}_3 \end{pmatrix}$, $\{R\} = \begin{pmatrix} \bar{R}_1 \\ \bar{R}_3 \end{pmatrix}$, $dV|_{V^e} = |\det[J^e]|d\xi_1 d\xi_2$. Let $\boldsymbol{x}^{(es)}$ and $\boldsymbol{x}^{(ef)}$ be the starting and final point, respectively, on $V^e$. Then, $d\Gamma|_{\Gamma^e} = \left|x^{(ef)} - x^{(es)}\right|/2\, d\xi_\nu = h^e(\xi)d\xi_\nu$ with $\xi_\nu \in [-1, 1]$ being the intrinsic variable along the side $\Gamma^e$ of the finite element $V^e$.

Now, let $(e_g c_g)$ be the global number of the node $\boldsymbol{x}^g$, $(g = 1, 2, \ldots, n)$. Since the variations of the independent field variables are arbitrary inside the analyzed domain and on its boundary, the last variational equation yields the system of algebraic equations

$$\begin{aligned} &\sum_{e_g}\sum_a\int_{-1}^1\int_{-1}^1\left\{\left([M^{e_g c_g}(\xi)]^T[\mathbf{C}]\left[M^{e_g a}(\xi)\right] + l^2\left[\Psi^{e_g c_g}(\xi)\right]^T[\mathbf{G}]\left[\Psi^{e_g a}(\xi)\right]\right)\right. \\ &\left\{q_u^{(e_g a)}\right\} - \left(\left[M^{e_g c_g}(\xi)\right]^T([\Lambda]\{v^{e_g a}(\xi)\} + [\Phi]\{\mu^{e_g a}(\xi)\})\right. \\ &\left.+\left[\Psi^{e_g c_g}(\xi)\right]^T[\mathbf{F}]^T\{v^{e_g a}(\xi)\} = \sum_{\substack{e_g \\ \Gamma^{e_g}\subset\Gamma_t^e}}\int_{-1}^1\{T(\xi)\}N^{c_g}(\xi)h^{e_g}(\xi)d\xi_\nu\right. \\ &\left.+\sum_{\substack{e_g \\ \Gamma^{e_g}\subset\Gamma_R^e}}\int_{-1}^1\{R(\xi)\}n_j(\xi)b_j^{e_g c_g}(\xi)h^{e_g}(\xi)d\xi_\nu\right)\phi^{(e_g a)}\Big\}\left|\det[J^{e_g}]\right|d\xi_1 d\xi_2 \end{aligned} \tag{60}$$

$$\begin{aligned} &\sum_{e_g}\sum_a\int_{-1}^1\int_{-1}^1\left\{\left(\{v^{e_g c_g}(\xi)\}^T([\Lambda]\left[\mathrm{M}^{e_g a}(\xi)\right] + [\mathbf{F}]\left[\Psi^{e_g a}(\xi)\right]\right)\right. \\ &\left.+\{\mu^{e_g c_g}(\xi)\}^T[\Phi]^T\left[\mathrm{M}^{e_g a}(\xi)\right]\right)\left\{q_u^{(e_g a)}\right\} \\ &+\left(\{v^{e_g c_g}(\xi)\}^T[\Pi]^T\{v^{e_g a}(\xi)\} + q^2\{\mu^{e_g c_g}(\xi)\}^T[\mathbf{H}]\{\mu^{e_g a}(\xi)\}\right)\phi^{(e_g a)}\Big\}\left|\det[J^{e_g}]\right|d\xi_1 d\xi_2 \\ &=\sum_{\substack{e_g \\ \Gamma^{e_g}\subset\Gamma_S^e}}\int_{-1}^1 S^-(\xi)N^{c_g}(\xi)h^{e_g}(\xi)d\xi_\nu \\ &+\sum_{\substack{e_g \\ \Gamma^{e_g}\subset\Gamma_Z^e}}\int_{-1}^1 Z^-(\xi)n_j(\xi)b_j^{e_g c_g}(\xi)h^{e_g}(\xi)d\xi_\nu \end{aligned} \tag{61}$$

The system of algebraic equations (60) - (61) can be applied for a general BVP described by the gradient theory with direct and converse flexoelectricity.

## 4. Numerical examples

A computer code for collocation MFEM based on the formulations presented in the previous sections has been developed in this study. To demonstrate its veracity, two example problems are presented here, namely, (a) a simple cantilever beam with a transverse end load, and (b) a truncated pyramid under compression.

### 4.1. A cantilever beam

Fig. 2 shows a cantilever beam subjected to a tansverse end load. With direct flexoelectricity, $q = 0$, $b_1 = b_2 = b_3 = 0$. For the analysis, it is treated as a 2D problem. A similar problem has been analyzed by Liang and Shen (2013) using the deformation asumptions of the Bernoulli-Euler beam theory.

The length of the beam is $L$ = 500 nm, the width is $B = 0.5H$ and the thickness is $H$ = 20 nm. The following boundary conditions are prescribed:

$$u_3|_{x_1=0} = 0, u_{3,1}|_{x_1=0} = 0, \int_A \tau_{111} x_3 dA = M^H\Big|_{x_1=0} = 0, M^H\Big|_{x_1=L} = 0$$

$$\left(M + P - M^H_{,1}\right)\Big|_{x_1=L} = 0, \frac{d}{dx_1}\left(M + P - M^H_{,1}\right)\Big|_{x_1=L} = Q \tag{62}$$

where $M = \int_A \sigma_{11} x_3 dA$ and $P = \int_A \tau_{113} dA$.

In this test problem, only direct flexoelectricity is considered. Analytical results are available only for this special case, derived by Liang and Shen (2013). The deflection of the cantilever beam with flexoelectricity is given by

$$u_3(x_1) = C_1 + C_2 x_1 + C_3 (x_1)^2 + C_4 (x_1)^3 + C_5 \exp\left(\frac{\lambda x_1}{L}\right) + C_6 \exp\left(-\frac{\lambda x_1}{L}\right) \tag{63}$$

$$\lambda^2 = \frac{\left[c_{11} I + \left(c_{11} l^2 + f_1 f_1 / a_{33}\right) A\right] L^2}{c_{11} l^2 I}$$

with $I$ as the second moment of cross-section area. The expression for $C_4$ in the work of Liang and Shen (2013) should be replaced by the correct one $C_4 = \frac{QL^2}{6\lambda^2 g_{11} I}$.

The corresponding theoretical solution for the flexoelectric field has also been given, and it is

$$E_3 = -\frac{f_1}{a_{33}} \eta_{113} = \frac{f_1}{a_{33}} \frac{d^2 u_3}{dx_1^2} \tag{64}$$

The piezoelectric material, PZT-5H is considered in this study.. The analytical solution for the cantilever beam is proposed for isotropic materials. To verify the results of the present collocation MFEM, the following isotropic material parameters are chosen: Young's modulus $E = 12.6 \times 10^{10}$Pa, Poisson's ratio $\nu = 0.2$, permittivity of the dielectric $a_{33} = 13.0 \times 10^{-9}$ C$^2$/N/m$^2$, internal material length $l$ = 2 nm.

First, the convergence of the present collocation MFEM is investigated, using the relative error e (x) for the $L^2$-norm:

$$e(\mathbf{X}) = \frac{\| \mathbf{X}^h - \mathbf{X} \|_{L^2}}{\| \mathbf{X} \|_{L^2}},$$

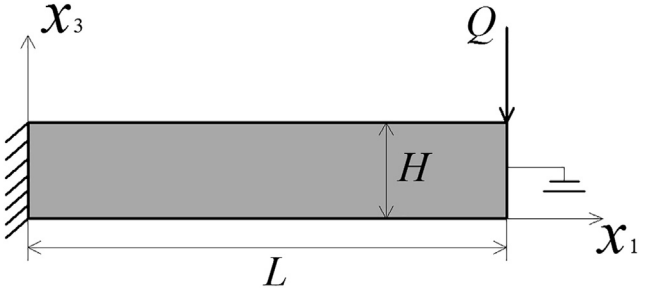


**Fig. 2.** Cantilever beam with shear force load.

where

$$\| \mathbf{X} \|_{L^2} = \left(\int_\Omega \mathbf{X}^{\mathrm{T}} \mathbf{X} d\Omega\right)^{1/2} \tag{65}$$

where $\mathbf{x}^h$ is the present collocation MFEM result, and $\mathbf{x}$ is the exact analytic solution. The relative errors for the beam deflection $u_3$ and the electric field $E_3$ are studied. There is, however, no exact analytical solution for the present flexoelectric beam problem. Thus, the approximate analytical solution of flexoelectric Bernoulli-Euler beam will be used here as x, where the shear stresses are neglected and all of the solutions are just a function of $x_1$. It should be reminded that the present 2D numerical solutions are functions of $x_1$ and $x_3$, which is closer to the actual physical situation.

The convergence of the present collocation MFEM is investigated using three different meshes with increasing refinement; they containing 320 elements, 900 elements and 1600 elements, respectively. Fig. 3 shows the relative errors for the deflection $u_3$ and electric field $E_3$ obtained using the three meshes for $f_1 = 1.0 \times 10^{-7}$C/m and $Q$ = 1nN, where $h$ is the average element length. The high convergence rates for both relative errors are clearly evident. In what follows, the most refined mesh mentioned above, with 1600 elements, is used for further numerical simulations of this beam problem.

The distribution of beam deflection $u_3$ along the cantilever beam for the load $Q$ = 1nN is presented in Fig. 4 with parameters $f_1 = 1.0 \times 10^{-7}$C/m and $f_2 = 0$. It is noted that the deflection increases gradually from the clamped end to the free end. In the present 2D numerical simulation, the deflection $u_3$ also vary along $x_3$, while it is just a function of $x_1$ in the analytical solution. A comparision of the deflections between the numerical solutions and the analytical solutions is presented in Fig. 5 for different flexoelectric coefficients ($f_1 = 0, f_1 = 1.0 \times 10^{-7}$C/m, $f_1 = 2.0 \times 10^{-7}$C/m, and $f_1 = 3.0 \times 10^{-7}$C/m). Excellent agreement between the numerical and analytical results is observed for various flexoelectric coefficients; the very small differences between them are due to assumptions in the analytical solution which yields a linear variation of normal stresses $\sigma_{11}$ along $x_3$ and vanishing shear stresses. In Fig. 5, it is also observed that the deflection of the beam decreases gradually as the flexoelectric coefficients increase in value. The classical beam theory predicts the largest deflection of the cantilever beam.

The distributions of electric responses inside the cantilever beam are presented in Fig. 6 for $f_1 = 1.0 \times 10^{-7}$C/m. The free-end of the beam is electrically grounded in the numerical simulations. Fig. 6(a) shows a non-uniform electric potential distribution inside the cantilever beam induced by direct flexoelectricity. The value of the electric potential decreases along the upper surface from the clamped-end to the free-end, while the inverse trend for it is shown on the lower surface of the beam. The distributions of the electric field $E_3$ are presented in Fig. 6(b). The electric field reaches its maximum at the clamped-end, where the strain gradient is the largest, thus resulting in maximum flexoelectricity. At the free-end of the cantilever beam, the electric field is zero, satisfying the electric boundary condition.

A comparision of the electric field $E_3$ between the numerical solutions and the analytical solutions for different flexoelectric coefficients are shown in Fig. 7. In the 2D numerical results, as expected, the electric field $E_3$ is not constant across the beam thickness; however, the average electric field value across the beam thicknes at each station along the beam is used for comparision with the analytical solution. It can be seen in Fig. 7 that the numerical solutions are in good agreement with the analytical results for different flexoelectric coefficients. There is no electro-mechanical transformation in classical beam theory, and vanishing electric

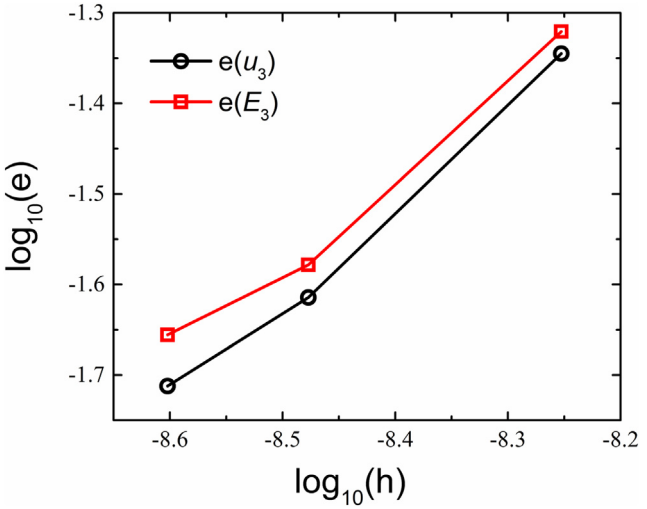


**Fig. 3.** Relative errors and convergence rates for the present collocation MFEM.


**Fig. 4.** Distributions of beam deflection $u_3$ (m) for the cantilever beam.

field is also seen here. From the present numerical simulation, it is also observed that the electric fields of the cantilever beam for $f_1$ = $2.0 \times 10^{-7}$C/m, and $f_1$ = $3.0 \times 10^{-7}$C/m are more significant when compared with $f_1$ = $1.0 \times 10^{-7}$C/m. From equation (64), it is noted that the electric field $E_3$ is determined by the flexoelectric coefficient and the strain gradient $\eta_{113}$ together. A linear growth of the electric intensity vector with the flexoelectric coefficient is moderated due to a rapid reduction of the strain gradient in (64).

*4.1.1. Dependence of flexoelectricity on the geometry of the cantilever beam*

In this section, the size dependence of flexoelectricity is first investigated by using the same orthotropic material, PZT-5H (Sladek et al., 2017, 2018) for the cantilever beam.

$$c_{11} = 12.6 \times 10^{10}\text{Pa}, c_{13} = 5.3 \times 10^{10}\text{Pa}, c_{33} = 11.7 \times 10^{10}\text{Pa}, c_{44} = 3.53 \times 10^{10}\text{Pa},$$

$$a_{11} = 15.1 \times 10^{-9}\text{C}^2/\text{N/m}^2, a_{33} = 13.0 \times 10^{-9}\text{C}^2/\text{N/m}^2,$$

$$f_1 = 1 \times 10^{-7}\text{C/m}, f_2 = 1 \times 10^{-7}\text{C/m} \quad (66)$$

Fig. 8 shows the average electric field distributions of the cantilever beam with five geometric sizes, where R is the size factor R = $L$/500 nm = $H$/20 nm = $Q$/1nN. Here, the material length parameter is taken to be $l$ = 2 nm and only the direct flexoelectric effect ($q = 0$, $b_1 = b_2 = b_3 = 0$) is analysed. It is noted that the electric field distributions of the beam have a similar trend for all of the five geometric sizes, and it is seen that the electric field gradually decreases from the clamped-end to the free-end. It indicates that larger strain gradients and stronger electro-mechanical coupling exist at the clamped-end of the cantilever beam. Additionally, it can also be observed that the the electric fields induced by flexoelectricity strongly depends on the geometric size of the cantilever

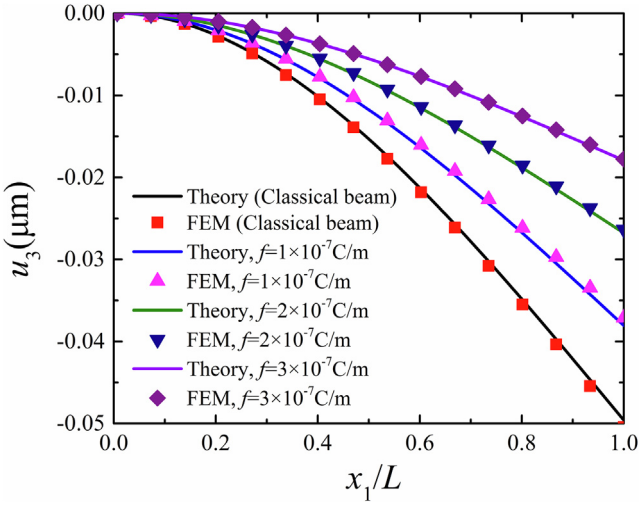


**Fig. 5.** Deflections of the cantilever beam with different flexoelectric coefficients.

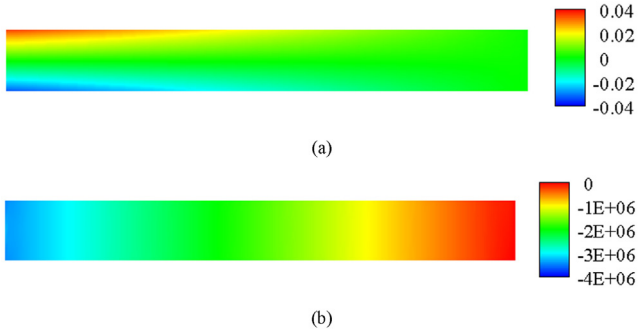


**Fig. 6.** Distributions of electric responses inside the cantilever beam. (a) the electric potential $\phi$(V), (b) the electric field $E_3$ (V/m).

beam. The magnitude of electric field is smaller in value for the larger sample size, and larger electric field is produced for reduced sample size. For example, the maximum value of electric field for R = 1 is about 2.5 times larger of that for R = 5. The apparent size effect of flexoelectricity is clearly evident in this cantilever beam example problem, demonstrating the well-known phenomenon of stronger flexoelectricity as the geometric size of the component decreases.

Another factor that may significantly affect the magnitude and distribution of the electric field is the shape of the cantilever beam. For given beam length $L$ = 500 nm, five beam thichnesses are considered to study the effect on flexoelectricity. The numerical results are shown in Fig. 9. The beam thichness $H$ are characterized by using the normalized thichness H* where $H$ = H* × 20 nm, and the corresponding load is $Q$ = H* × 1nN. From Fig. 9, it can be observed that the electric field distributions monotonously decrease from the clamped-end to the free-end for the cantilever beam with different thicknesses. It is also noted that smaller H* results in larger electric field. For example, the maximum value of electric field for H* = 1 is about 10 times larger of that for H* = 5. The results indicate that the electric fields increase with decreasing H*. This is consistent with the fact that thinner beam leads to larger strain gradients, thus, stronger flexoelectricity.

*4.2. A truncated pyramid*

A truncated pyramid under a compression is another good flexoelectric example that has been extensively studied experimen-

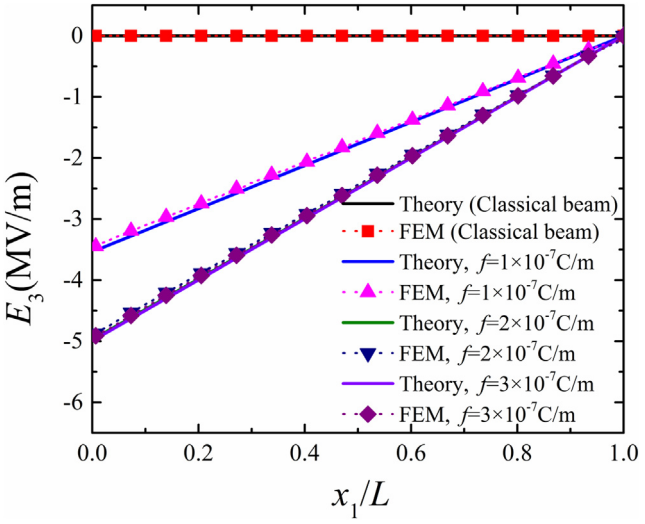


**Fig. 7.** Electric field of the cantilever beam with different flexoelectric coefficients.

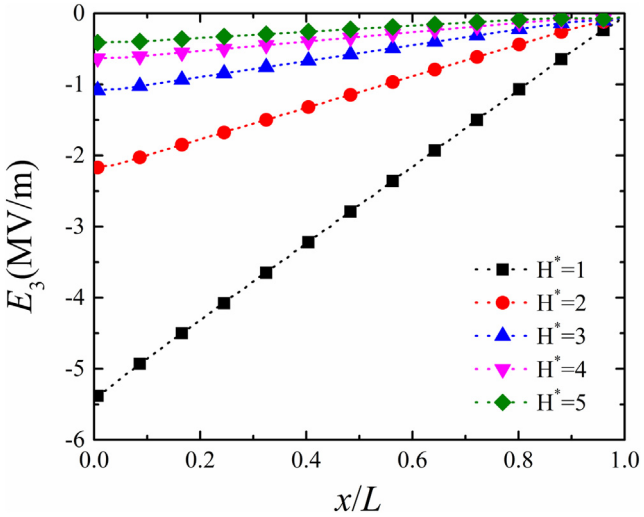


**Fig. 9.** Electric field distributions of the cantilever beam with five various thicknesses.

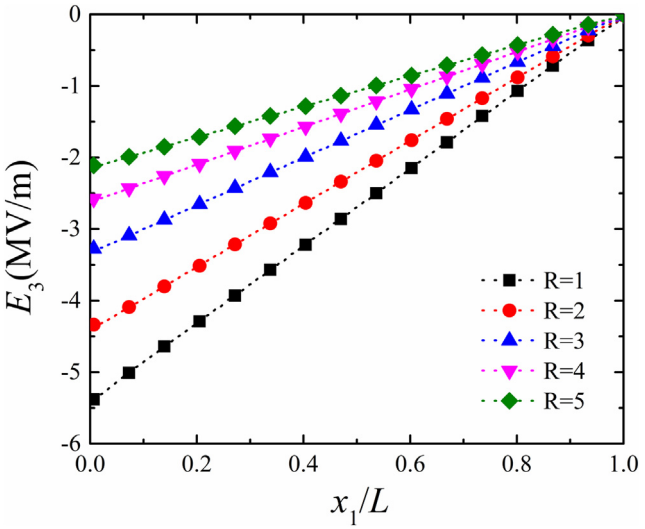


**Fig. 8.** Electric field distributions of the cantilever beam with five geometric sizes.

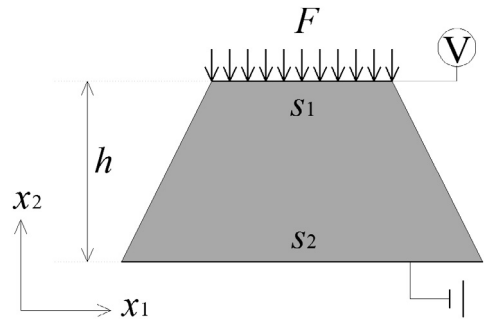


**Fig. 10.** Schematic of a truncated pyramid.

tally and theoretically (Cross, 2006). Numerical simulations can also be found in some works (Abdollahi et al., 2014; Codony et al., 2019; Zhuang et al., 2020). Fig. 10 shows the geometry of a truncated pyramid with top surface $s_1$, bottom surface $s_2$, and height $h$. The electric boundary conditions are prescribed as follows: the bottom surface is grounded with zero electric potential and an electrode is attached to the top surface that results in an equipotential value there. The mechanical boundary conditions are: a uniform total load $\boldsymbol{F}$ is applied on the top surface with the bottom surface rigidly supported against vertical displacement, i.e., $u_2 = 0$. Due to the different lengths of the top surface and bottom surface, a longitudinal strain gradient is produced resulting in flexoelectric polarization. In Cross' study (Cross, 2006), the effective piezoelectric constant $d_{\text{eff}}$ of the truncated pyramid is simplified as

$$d_{\text{eff}} = f_1\left(\frac{s_2 - s_1}{h s_1}\right) \tag{67}$$

Note that the effective piezoelectric constant $d_{\text{eff}}$ in Eq. (67) is size-dependent. Plane strain condition is assumed in the 2D collocation MFEM analysis. The material constants of PZT-5H in Eq. (66) are also used here with $q = 0$, $b_1 = b_2 = b_3 = 0$, being interested in the direct flexoelectric effect. In the numerical simulations, the electric potential $V$ on the top surface is unknown *a priori* but is a constant. With the resulting $V$, the effective piezoelectric constant $d_{\text{eff}}$ can be calculated as (Abdollahi et al., 2014)

$$d_{\text{eff}} = \frac{a_{33}E_2}{\varepsilon_{22}} = \frac{a_{33}Vs_2c_{11}}{hF} \tag{68}$$

Fig. 11 shows the effective piezoelectric constant $d_{\text{eff}}$ of the truncated pyramid as a function of the normalization parameters $h/h_0$, keeping $s_1 = h = s_2/2$ and $h_0 = 20$ μm. For this model, the material length parameter is taken to be $l = 2$ μm. Good agreement is obtained between the theoretical estimates using Eq. (67) and the present collocation MFEM results. As discussed in the cantilever beam problem earlier, the small difference between the theoretical and the numerical results is due to the 2D effect, which is simplified to 1D in the analytical solution. From Fig. 11, it can be seen that the effective piezoelectric constant $d_{\text{eff}}$ increases with decreasing values of the the normalization parameter $h/h_0$. An apparent size-dependent effective piezoelectric constant $d_{\text{eff}}$ is observed for the present truncated pyramid model without piezoelectricity. The distributions of mechanical fields (longitudinal displacement $u_2$ and longitudinal strain $\varepsilon_{22}$) and flexoelectric responses (electric potential $\phi$ and longitudinal electric field $E_2$) are shown in Fig. 12. The results shown are obtained for

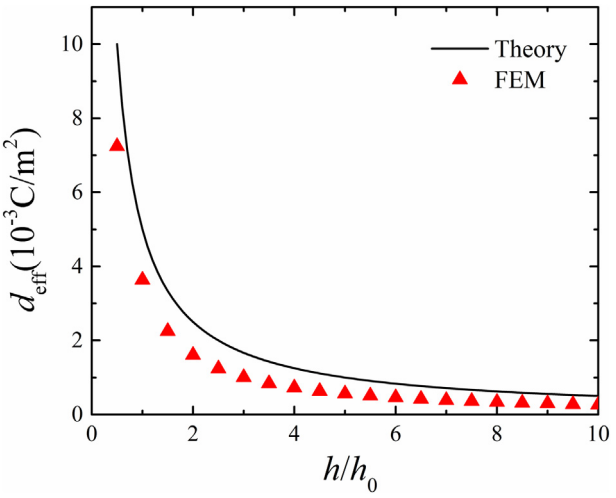


**Fig. 11.** Effective piezoelectric constant $d_{eff}$ as a function of the normalization parameters $h/h_0$, where the aspect ratio of the truncated pyramid is $s_1 = h = s_2/2$ and $h_0 = 20$ μm.

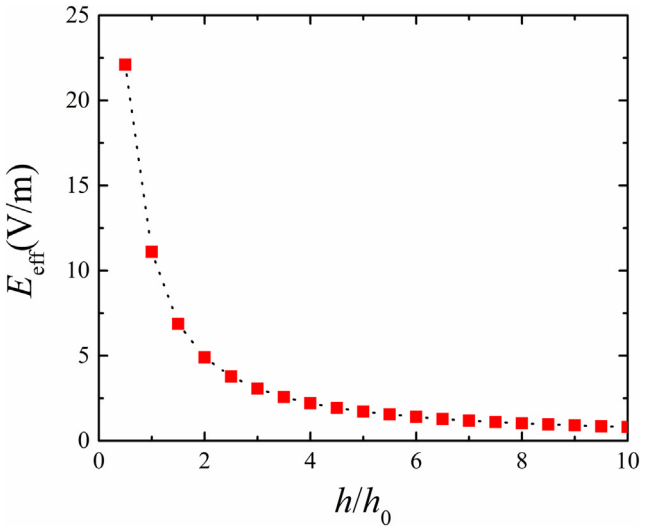


**Fig. 13.** Effective electric field $E_{eff}$ as a function of the normalization parameters $h/h_0$, where the aspect ratio of the truncated pyramid is $s_1 = h = s_2/2$ and $h_0 = 20$ μm.

$h = 20$ μm and $\boldsymbol{F} = 200$ N. In can be seen in Fig. 12(b) that the longitudinal strain distributions are non-uniform, and significant strain gradients exist inside the truncated pyramid. The corresponding electric potential distributions are shown in Fig. 12(c); the electric boundary conditions are clearly satisfied, namely, the electric potential is zero on the bottom surface and the equipotential value is 0.22 mV on the top surface. The longitudinal electric field distributions are plotted in Fig. 12(d), and the electric field $E_2$ is larger near the pyramid corners due to the strong stress concentration accompanied with larger strain gradients.

*4.2.1. Dependence of flexoelectricity on the geometry of the truncated pyramid*

In this section, the effects of geometric size and shape factor of the truncated pyramid model on flexoelectricity are studied. To evaluate the flexoelectric response, the effective electric field $E_{eff}$ is defined as follows.

$$E_{eff} = \frac{\Delta V}{h} \tag{69}$$

where $\Delta V$ represents the voltage difference between the the top surface and the bottom surface of the truncated pyramid, and $h$ is its height.

For a given aspect ratio of the truncated pyramid model $s_1 = h = s_2/2$, changing $h$ would lead to the change of $s_1$ and $s_2$ at the same time. Fig. 13 shows the variation of the effective electric field $E_{eff}$ with the normalization parameter $h/h_0$, where $h_0 = 20$ μm, and a total load 10 MPa is uniformly applied on the top surface. It can be observed that the effective electric field $E_{eff}$ is larger for a reduced sample size. This is in agreement with the results reported in the literature (see, e.g., Deng, 2017; Codony et al., 2019). Similar to the cantilever beam problem above, size-dependent flexoelectricity is evident in this truncated pyramid model as well.

To further understand the effect of shape factor on flexoelectricity, the aspect ratio $s_2 : h : s_1 = 1 : 0.5 : R$, is kept the same. Thus, for

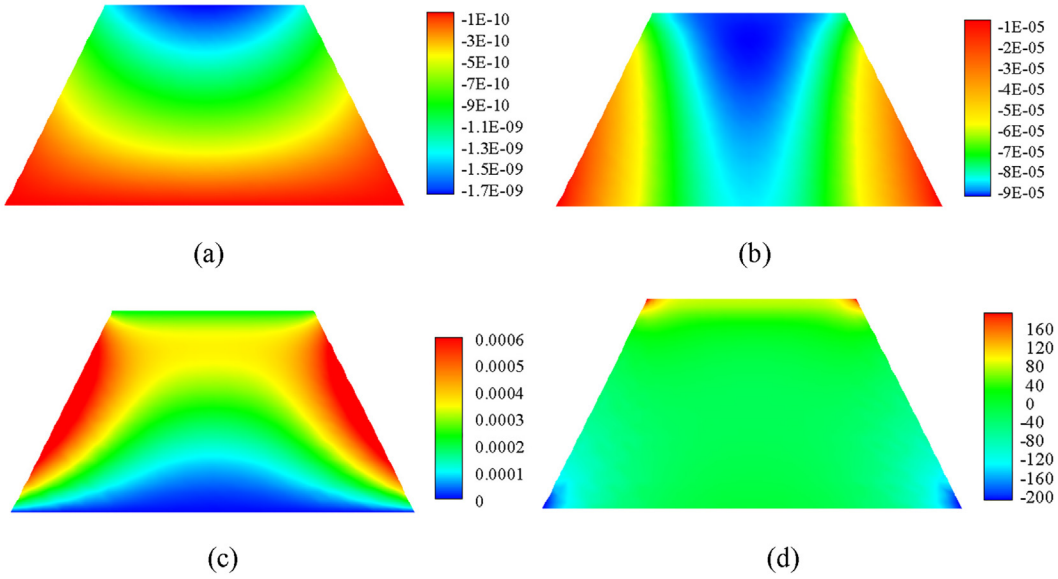


**Fig. 12.** Distributions of mechanical fields and flexoelectric responses under uniform load on the top surface and rigid support on the bottom surface, the bottom surface is grounded and an electrode is attached on the top surface. (a) longitudinal displacement $u_2$ (m), (b) longitudinal strain $\varepsilon_{22}$, (c) the electric potential $\phi$(V), (d) the electric field $E_2$ (V/m).

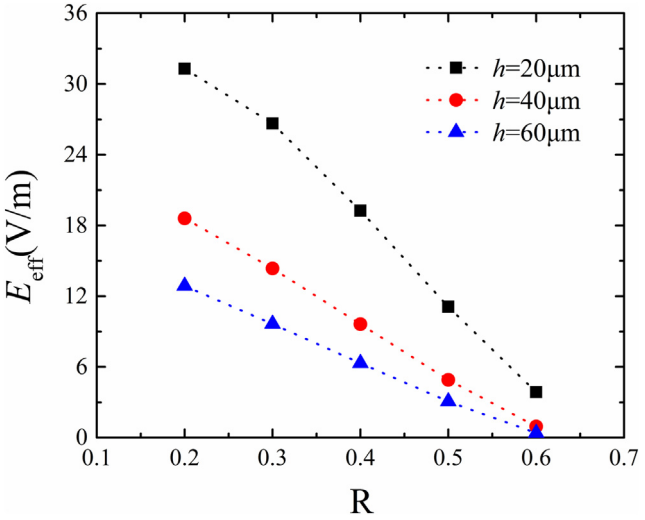


**Fig. 14.** Effective electric field $E_{\text{eff}}$ of the truncated pyramid with different aspect ratios, where $s_2 : h : s_1 = 1 : 0.5 : R$.

a given heigh $h$, the bottom length $s_2$ is confirmed. Changing R would lead to the change of the top length $s_1$. As shown in Fig. 14, three values of $h$ = 20 μm, 40 μm, and 60 μm, respectively are chosen to study the shape effects on the effective electric field $E_{\text{eff}}$ of the truncated pyramid with a uniform load 10 MPa on the top surface. The effective electric field $E_{\text{eff}}$ is found to increase with decreasing value of R for all these three cases. As a smaller R value result in a larger difference between $s_1$ and $s_2$; this leads to larger strain gradients which produce a stronger flexoelectric effect inside the truncated pyramid.

## 5. Conclusions

In this paper, the governing equations with direct and converse flexoelectricity have been derived. A collocation MFEM formulation was presented and a 2D element also developed to solve standard BVPs in flexoelectricity. In this collocation MFEM formulation, $C^0$ continuous approximation was applied for independent displacement, strain, electric potential and electric intensity vector variables. The kinematic constraints between primary fields (displacements, potential) and secondary fields (strain, electric intensity) are satisfied by a collocation method at judiciously chosen internal points in the elements. This scheme significantly reduces the number of the DOFs when compared to the traditional Lagrangian approach, and at the same time, the kinematic constraints between the displacement and strain are guaranteed. The corresponding 2D collocation MFEM code has also been developed. Two example problems have also been presented to demonstrate its veracity for obatining accurate and convergent solutions. In the first example, namely, a cantilever beam subject to an end load, both the deflection and the electric response obtained were in in good agreement with the results from theoretical solutions. In the second example of a truncated pyramid, good agreement of the effective piezoelectric constant with available solution in the literature was also obtained. The size-dependence of flexoelectricity was successfully predicted for both these two example problems using the collocation MFEM developed in this study. Larger aspect ratios of the physical dimensions of the solid body lead to larger strain gradients and flexoelectricity. The collocation MFEM formulation developed in this paper can be applied to, for example, structural health monitoring of flexoelectric sensors or actuators.

## Declaration of Competing Interest

The authors declare that they have no known competing financial interests or personal relationships that could have appeared to influence the work reported in this paper.

## Acknowledgements

This work was supported by the National Key R&D Program of China (2017YFE0119800). The authors acknowledge the supports by the Slovak Science and Technology Assistance Agency registered under number SK-CN-RD-18-0005 and VEGA-2/0061/20.

## References

Abdollahi, A., Millan, D., Peco, C., Arroyo, M., Arias, I., 2015. Revisiting pyramid compression to quantify flexoelectricity: A three-dimensional simulation study. Phys. Rev. B 91, 104103.
Abdollahi, A., Peco, C., Millan, D., Arroyo, M., Arias, I., 2014. Computational evaluation of the flexoelectric effect in dielectric solids. J. Appl. Phys. 116, 093502.
Amanatidou, E., Aravas, N., 2002. Mixed finite element formulations of strain-gradient elasticity problems. Comput. Method. Appl. M. 191, 1723–1751.
Bishay, P.L., Sladek, J., Sladek, V., Atluri, S.N., 2012. Analysis of functionally graded multiferroic composites Using Hybrid/Mixed Finite Elements and Node-Wise Material Properties. CMC 29, 213–262.
Codony, D., Marco, O., Fernández-Méndez, S., Arias, I., 2019. An immersed boundary hierarchical B-spline method for flexoelectricity. Comput. Method. Appl. M. 354, 750–782.
Cross, L.E., 2006. Flexoelectric effects: Charge separation in insulating solids subjected to elastic strain gradients. J. Mater. Sci. 41, 53–63.
Deng, F., Deng, Q., Yu, W., Shen, S., 2017. Mixed finite elements for flexoelectric solids. J. Appl. Mech. 84, 081004.
Deng, F., Deng, Q., Shen, S.P., 2018. A three-dimensional mixed finite element for flexoelectricity. J. Appl. Mech. 85, 031009–31011.
Deng, Q., 2017. Size-dependent flexoelectric response of a truncated cone and the consequent experimental measurement of flexoelectric properties. J. Appl. Mech. 84, 101007–101011.
Deng, Q., Liu, L., Sharma, P., 2014a. Flexoelectricity in soft materials and biological membranes. J. Mech. Phys. Solids 62, 209–227.
Deng, Q., Liu, L., Sharma, P., 2014b. Electrets in soft materials: Nonlinearity, size effects, and giant electromechanical coupling. Phy. Rev. E. 90, 012603.
Deng, Q., Lv, S., Li, Z., Tan, K., Shen, S., 2020. The impact of flexoelectricity on materials, devices, and physics. J. Appl. Phys. 128, 080902.
Dong, L., Atluri, S.N., 2011. A simple procedure to develop efficient & stable hybrid/mixed elements, and Voronoi cell finite elements for macro- & micromechanics. CMC 24, 61–104.
Gharbi, M., Sun, Z.H., Sharma, P., White, K., 2009. The origins of electromechanical indentation size effect in ferroelectrics. Appl. Phys. Lett. 95, 142901.
Gitman, I., Askes, H., Kuhl, E., Aifantis, E., 2010. Stress concentrations in fractured compact bone simulated with a special class of anisotropic gradient elasticity. Int. J. Solids Struct. 47, 1099–1107.
Harris, P., 1965. Mechanism for the shock polarization of dielectrics. J. Appl. Phys. 36, 739–741.
Hu, S.L., Shen, S.P., 2009. Electric field gradient theory with surface effect for nano-dielectrics. CMC 13, 63–87.
Krichen, S., Sharma, P., 2016. Flexoelectricity: A perspective on an unusual electromechanical coupling. J. Appl. Mech. 83, 030801–30811.
Kogan, S.M., 1964. Piezoelectric effect during inhomogeneous deformation and acoustic scattering of carriers in crystals. Sov. Phys. Solid State 5, 2069–2070.
Lekhnitskii, S.G., 1963. Theory of Elasticity of an Anisotrophic Elastic Body. Holden-Day.
Liang, X., Shen, S., 2013. Size-dependent piezoelectricity and elasticity due to the electric field-strain gradient coupling and strain gradient elasticity. Int. J. Appl. Mech. 5, 1350015.
Liu, C., Wang, J., Xu, G., Kamlah, M., Zhang, T.Y., 2019. An isogeometric approach to flexoelectric effect in ferroelectric materials. Int. J. Solids Struct. 162, 198–210.
Ma, W., Cross, L.E., 2001. Large flexoelectric polarization in ceramic lead magnesium niobate. Appl. Phys. Lett. 79, 4420–4422.
Ma, W., Cross, L.E., 2006. Flexoelectricity of barium titanate. Appl. Phys. Lett. 88, 2004–2007.
Mao, S., Purohit, P.K., Aravas, N., 2016. Mixed finite-element formulations in piezoelectricity and flexoelectricity. P. R. Soc. A Math. Phy. 472, 20150879.
Maranganti, R., Sharma, N.D., Sharma, P., 2006. Electromechanical coupling in nonpiezoelectric materials due to nanoscale nonlocal size effects: Green's function solutions and embedded inclusions. Phys. Rev. B 74, 014110.
Maugin, G.A., 1980. The method of virtual power in continuum mechanics: Applications to coupled fields. Acta Mech. 35, 1–80.
Meyer, R.B., 1969. Piezoelectric effects in liquid crystals. Phys. Rev. Lett. 22, 918–921.

Mohammadi, P., Liu, L., Sharma, P., 2014. A theory of flexoelectric membranes and effective properties of heterogeneous membranes. J. Appl. Mech. 81, 011007–11012.
Nguyen, B., Zhuang, X., Rabczuk, T., 2018. Numerical model for the characterization of Maxwell-Wagner relaxation in piezoelectric and flexoelectric composite material. Comput. Struct. 208, 75–91.
Nguyen, B., Zhuang, X., Rabczuk, T., 2019. NURBS-based formulation for nonlinear electro-gradient elasticity in semiconductors. Comput. Method. Appl. M. 346, 1074–1095.
Parton, V.Z., Kudryavtsev, B,A., 1988. Electromagnetoelasticity: piezoelectrics and electrically conductive solids, Taylor & Francis.
Rahmati, A.H., Yang, S., Bauer, S., Sharma, P., 2019. Nonlinear bending deformation of soft electrets and prospects for engineering flexoelectricity and transverse ($d_{31}$) piezoelectricity. Soft. Matter. 15, 127–148.
Sharma, P., Maranganti, R., Sharma, N.D., 2006. Electromechanical coupling in nanopiezoelectric materials due to nanoscale nonlocal size effects: Green function solution and embedded inclustions. Phys. Rev. B 74, 014110.
Shen, S.P., Hu, S.L., 2010. A theory of flexoelectricity with surface effect for elastic dielectrics. J. Mech. Phys. Solids 58, 665–677.
Sladek, J., Sladek, V., Stanak, P., Zhang, Ch., Tan, C.L., 2017. Fracture mechanics analysis of size-dependent piezoelectric solids. Int. J. Solids Struct. 113, 1–9.
Sladek, J., Sladek, V., Wunsche, M., Zhang, C., 2018. Effects of electric field and strain gradients on cracks in piezoelectric solids. Eur. J. Mech. A-Solid. 71, 187–198.
Sladek, J., Stanak, P., Han, Z.D., Sladek, V., Atluri, S.N., 2013. Applications of the MLPG method in engineering & Sciences: A review. CMES-Comp. Model. Eng. 92, 423–475.
Tagantsev, A.K., 1986. Piezoelectricity and flexoelectricity in crystalline dielectrics. Phys. Rev. B 34, 5883–5889.
Tagantsev, A.K., Meunier, V., Sharma, P., 2009. Novel electromechanical phenomena at the nanoscale: phenomenological theory and atomistic modelling. MRS Bullet. 34, 643–647.
Thai, T.Q., Rabczuk, T., Zhuang, X., 2018. A large deformation isogeometric approach for flexoelectricity and soft materials. Comput. Method. Appl. M. 341, 718–739.
Wang, B., Gu, Y., Zhang, S., Chen, L.Q., 2019. Flexoelectricity in solids: Progress, challenges, and perspectives. Prog. Mater. Sci. 106, 100570.
Yaghoubi, S.T., Mousavi, S.M., Paavola, J., 2017. Buckling of centrosymmetric anisotropic beam structures within strain gradient elasticity. Int. J. Solids Struct. 109, 84–92.
Yang, X.M., Hu, Y.T., Yang, J.S., 2004. Electric field gradient effects in anti-plane problems of polarized ceramics. Int. J. Solids Struct. 41, 6801–6811.
Yudin, P., Tagantsev, A., 2013. Fundamentals of flexoelectricity in solids. Nanotechnology 24, 432001.
Yvonnet, J., Liu, L., 2017. A numerical framework for modeling flexoelectricity and maxwell stress in soft dielectrics at finite strains. Comput. Method. Appl. M. 313, 450–482.
Zhuang, X., Nguyen, B.H., Nanthakumar, S.S., Thai, T.Q., Alajlan, N., Rabczuk, T., 2020. Computational modeling of flexoelectricity – A review. Energies 13, 1326.